Mechanically Activated Covalent Organic Framework as Metal Free Photocatalyst for Continuous Flow Fenton-like Degradation of Organic Pollutants and Hexavalent Chromium Reduction

Rituporn Gogoi[a], Swadhin Kumar Jena[a], Astha Singh[a], Kajal Sharma[a], Kirti Khanna[a], Sumanta Chowdhury[a], Rajesh Kumar[a], and Prem Felix Siril*[a]

[a]School of Chemical Sciences, Indian Institute of Technology Mandi, Mandi, Himachal Pradesh-175005, India
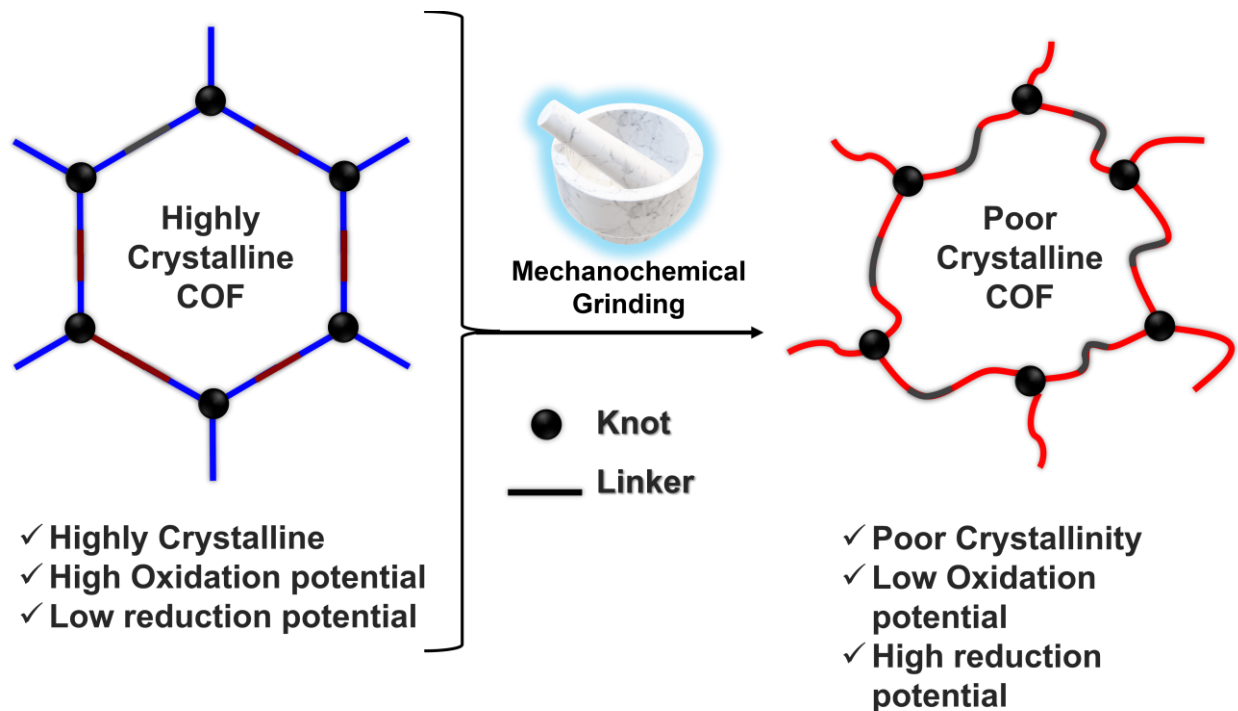
*Corresponding author: prem@iitmandi.ac.in

Graphical abstract

Highlights

1. Highly activated photocatalyst unveiled via mechanical pulverization of covalent organic framework.

2. Increased COF excited electron density through pulverization allows for efficient stable electron and hole separation to produce highly reactive species.

3. A metal free, heterogeneous photocatalyst both for photoreduction of Cr^{6+} and Fenton-like reactions under visible light.

4. An outstanding activity for photo Fenton-like degradation of organic pollutants (apparent quantum yield of 41%) at significantly low concentrations of H_2O_2 and COF under very short period.

5. Continuous flow photocatalytic degradation showed twenty-eight times higher activity for Fenton-like reactions.

Graphical abstract

Highly Crystalline COF → Mechanochemical Grinding → Poor Crystalline COF

● Knot

— Linker

Highly Crystalline COF
✓ Highly Crystalline
✓ High Oxidation potential
✓ Low reduction potential

Poor Crystalline COF
✓ Poor Crystallinity
✓ Low Oxidation potential
✓ High reduction potential

24 **Abstract**

25 A highly active photocatalyst is unveiled for the Fenton-like reactions in visible light. A metal free
26 covalent organic framework (COF) was highly active via a novel mechanical pulverization process.
27 Under visible light, the activity of pulverized COF reached the apparent quantum yield up to 41%
28 for Fenton-like degradation. The exceptional performance is due to the induced high excited
29 electron density at conduction band. The outstanding performance does not require to adjust pH
30 by external means unlike the metal based photocatalysts. The pulverized COF can be recycled up
31 to five times. The photocatalyst outperformed in continuous flow channel for industrial scale
32 implementation. The photocatalytic space time yield (PSTY) was highly improved by twenty-eight
33 times than the conventional batch photocatalysis. A very low amount of photocatalyst requires
34 very low alone is sufficient for bring successful chemical reactions. Additionally, a very high
35 photoreduction rate was also observed for hexavalent chromium which was significantly better
36 than the parent COF.

37 **Keywords:** Mechanical grinding, Photo Fenton-like reaction, chromium reduction, Covalent
38 organic Framework, Photocatalysis.

39 **Introduction**

40 Anthropogenic pollutants are being utilized in many different sectors, such as the textile, paper,
41 plastics, and leather industries. Their toxicity and mutagenetic effects on living beings are very
42 severe. Of this kind pollutants, biodegradation or natural remediation is incredibly slow and has
43 little to no effect on their longevity. As one of the most promising advanced oxidation processes,
44 Fenton reactions are instead frequently used in the control of industrial effluent and pollutants

45 (AOPs). Fenton like reactions produce highly reactive species, ($\cdot$OH, $SO_4^{\cdot-}$, $O_2^{\cdot-}$ or $^1O_2$) via
46 activation of several radical initiators as hydrogen peroxide (H_2O_2), peroxymonosulfate (PMS) and
47 peroxydisulfate (PDS). A broad range of metallic or semiconducting materials or the composite
48 nanomaterials are employed for the efficient removal of organic pollutants using Fenton-like
49 reaction. The use of metal-based photocatalysts is restricted due to the metal leaching. Because of
50 their expensive nature and negative effects, using them can occasionally be harmful to human
51 health.[1] Metal-free catalytic systems are greatly desired for wastewater treatment due to their
52 simplicity, low environmental effect, and practicability. Fenton-like reactions with metal-free
53 photocatalysts have recently been discovered to be a viable method for cleaning up organic
54 contaminants. Unlike the metal-based approaches, metal free system operates in broad range of
55 pH scale and avoids the risk of metal leaching.[2] Additionally, heterogeneous metal-free catalysts
56 are easily isolated from the reaction mixtures and readily employed for numerous cycles, saving
57 energy, time, and labor while preparing the photocatalysis in contrast to homogenous. Only a
58 limited photocatalyst are reported for Fenton-like reactions that produce reactive radicals under
59 visible light. For instance, multiwalled carbon nanotubes (MWCNT),[3] reduced graphene oxide,[4]
60 graphitic carbon nitride,[5] and photoelectron-Fenton like cell,[6] and COF-THTBD.[7] Among them,
61 triazine linked Tp-Mela COF is reported as highly active photo Fenton-like activities over several
62 colored and colorless pollutants. The efficiency of the Tp-Mela COF photocatalyst is much higher
63 even than several metal-based photo Fenton-like systems.[2]

64 Covalent organic frameworks (COF) are a class of surprisingly unique class of materials which
65 are environmentally friendly carbonaceous materials. Owing to the ordered porosity and extremely
66 high porosity, COFs are recently gained much attention over a wide range of applications such as
67 adsorption, separation/purification, and catalysis (electro, photo-,[8] and electrochemical).
68 Additionally, the visible light absorbing semiconducting properties in COF materials additionally
69 blown up the interests in several optoelectronic applications especially in metal photocatalysis.
70 However, the inherent properties of such a wonder material are still unexplored specially for the
71 of COF materials. However, the notion of extended conjugation, decreased electron-hole
72 recombination, and suppressed photo-corrosion are the only known strategies for improving the
73 photocatalytic activities of novel COF-based materials. This includes functional group or side
74 chain modulation,[9] elemental doping of non-metals[10] and metals[11] incorporation of light
75 sensitizing co-catalyst[12], nanoconfining,[13] construction of hybrid structures are believed to provide
76 versatile strategies for improved photocatalysis.[14] Through effective charge carrier separation and
77 hence mobility, COF materials can be carefully designed to easily improve photocatalytic
78 performance.

79 Mechanical stimuli are alternative techniques that often-reported changes optical properties of
80 semiconducting materials. The molecular packing of materials is easily altered under application
81 of mechanical stimuli and thus optical band positions of materials.[15] Application of an external
82 stimuli includes shearing, grinding[16] or rubbing, results reversibly or irreversibly undergo
83 planarization of twisted conformation as a result in changed absorbance or emission properties.[17]

84 As a proof of concept, we prepared anthraquinone incorporated COF which was mechanically
85 pulverized and showed highly efficient photocatalytic activities for decontamination
86 environmental pollutants. The photophysical properties of the pulverized COF showed the highly
87 efficient electron and hole separation and transfer abilities as compared to the pristine COF.
88 Accordingly, we observed highly appealing results in photo Fenton-like degradation for
89 decontamination of organic pollutants as well as photoreduction of carcinogenic strong inorganic
90 oxidants (here, hexavalent chromium). The activity of the pulverized COF reaches the apparent
91 quantum yield up to 41% for Fenton-like degradation even at very low concentrations. As per the
92 author knowledge, the photo Fenton-like activities of pulverized COF is highest amongst the
93 reported literatus so far. The outstanding performance of the metal free photocatalyst does not
94 require to adjust pH by external means unlike the metal based photocatalysts. The superior
95 activities with several times of recyclability additionally demonstrated an indispensable
96 photocatalysts could be obtained via the pulverization technique. Furthermore, the photocatalyst
97 outperformed in a continuous flow reactor, demonstrated the photocatalyst could be a viable
98 candidate for long-term industrial scale implementation. Additionally, a very high photoreduction
99 rate was also observed for hexavalent chromium which was significantly better than the parent
100 COF without application of external sacrificial agents.

101 **Materials and reagents**

102 2,6-Diaminoanthraquinone (97.0%, DAAQ), rhodamine B (>98.0 %(T), RB) and crystal violet
103 hydrate dyes were purchased from Tokyo Chemical Industry (TCI Chemicals).
104 Hexamethylenetetramine (>99 %, HMTA) was procured from Alfa Aesar and phloroglucinol
105 (98 %) was purchased from Avra. Methylene blue was purchased from Rankem, methyl orange
106 (>98.0 %, MO) from Merck Life Science Private Limited India. 1,5-Diphenylcarbazide, sodium
107 azide (NaN_3), coumarin (≥99%, HPLC), ethylenediaminetetraacetic acid disodium salt (EDTA-
108 2Na), potassium dichromate ($K_2Cr_2O_7$), sodium hydroxide (ACS reagent, ≥97.0 %, NaOH pellets),
109 and reagent grade p-Benzoquinone (≥98% purity, p-BQ) were purchased from Sigma-Aldrich.
110 Trifluoroacetic acid (>99.0%, TFA), dichloromethane (>99.5 %, DCM), tert-butyl alcohol (TBA)
111 and N, N-dimethylformamide (99.5%, DMF) were purchased from SRL Chemicals. Acetone and
112 isopropyl alcohol (IPA) were purchased from SD Fine Chemical Ltd. Glacial acetic acid (Reagent
113 Plus® ≥ 99 %) from CDH fine chemical, India pvt. Ltd, sulfuric acid (H_2SO_4), hydrochloric acid
114 (HCl, 35-38%) and hydrogen peroxide (30%, H_2O_2) were from SD Fine Chem Ltd (SDFCL).
115 Absolute grade ethanol was purchased from CDS Analytical. Ultrapure water (Millipore System,
116 18.2 MΩ cm) was used until and unless specified otherwise. The connections in flow channels
117 were established using silicon-based tubing (0.8 mm ID), which was purchased from Polymax
118 Elastomers Pvt. Ltd. All the reagents are commercially available, analytically pure and used as
119 received without further purification.

120 **Characterization**

121　The materials were carefully characterized using a variety of sophisticated techniques. Rigaku
122　SmartLab 9 kW rotating anode set with Bragg-Brentano configuration was used to acquire the
123　powder X-ray diffraction (pXRD) data. The setup used a Cu-sealed tube (Cu K X-rays of 0.1542
124　nm) that worked at 100 mA and 45 kV. The scattering range for the samples was 3 to 50° while
125　the scan rate was 2° per minute (step size: 0.02°). The Fourier transform infrared spectra (FT-IR)
126　were recorded using Perkin Elmer spectrum Two attached with $LaTiO_3$ MIR detector. Spectra
127　were acquired in the range of 4000-400 cm^{-1}. The NMR spectrum in the solid state (SS-NMR) was
128　recorded using Bruker AVANCE HD 500MHz FT-NMR spectrometer, equipped with 4 mm
129　broadband CP-MAS solid probe. The samples were loaded into the instrument inside of a zirconia
130　rotor (4 mm). During the analysis, a magnetic field of 11.7 T was externally applied. By using
131　linearly ramped cross-polarization with Magic-angle spinning (CP-MAS) at 125.79 MHz, ^{13}C
132　NMR spectra was evaluated. The CP contact time, flip angle, and pulse width were all set at 2 ms,
133　90°, and 3.84 s, respectively. The material was assessed using 2048 scans with a 3 s recycle delay.
134　Thermogravimetric analysis (TGA) was performed using Perkin Elmer Pyris 1 instrument in the
135　temperature range of 25-600 °C. The samples were loaded on a Pt crucible and heated at the rate
136　of 5 °C min^{-1} while being subjected to N_2 gas at the flow rate of 20 mL min^{-1}. The nitrogen gas
137　adsorption-desorption isotherms at 77 K were recorded in a Quanta chrome Autosorb-iQ-MP/XR
138　system to assess the Brunauer-Emmett-Teller (BET) surface area. Particle morphology of the
139　samples were imaged using high-resolution transmission electron microscopy (HRTEM, FEI
140　Tecnai G2 20 S-twin electron microscope, operated at 200 kV) and field emission scanning
141　electron microscopy (FESEM, FEI Nova Nano SEM-450 coupled with Ametek make EDS).
142　Thermo Scientific Nexsa surface analyzer, which was equipped with an Al-k source (with a
143　wavelength of 0.83 nm), was used to obtain X-ray photoelectron spectra (XPS). The filament
144　current and anode voltage were set at 6.03 mA and 1200 V, respectively. All the spectra were
145　acquired with a pass energy of 50 eV and step size 0.1 eV. The narrow scan spectra of all the
146　components were deconvoluted using Avantage 5.9908 curve fitting software. A modified Shirley
147　background that applies additional limitations to maintain background intensity lower than the
148　actual data at any point in the region was used for deconvolution. Adventitious carbon (284.8
149　eV) was used as a reference point. Ultraviolet photoelectron spectra (UPS) were acquired using
150　He I excitation (21.2 eV) produces ultraviolet photons (gas discharge lamp). The UV-Vis
151　absorbance spectra were acquired using Simadzu UV-2450 spectrophotometer. Steady state
152　photoluminescence (PL) emission spectra were recorded on a Horiba flourolog-3 using a quartz
153　cell (1 cm) with 5/5 slit widths. The time resolved fluorescence lifetime was measured using a
154　Pulsed LED source-equipped with Delta Flex system from Horiba Scientific. To obtain lifetime,
155　the photon decays in various channels were fitted using bi-exponential equation with a chi-squared
156　value ~1.2. The photocatalytic activities were examined under visible lights using a custom-built
157　photoreactor made of 100W RGB Hi-Bay LED lights from Oreva. The intensities of LEDs were
158　measured by using a OAI solar meter with illumination area of 4 cm^2 (2 × 2 cm). The reaction
159　temperature in the photoreactor was carefully measured using a non-contact digital laser infrared
160　thermometer (HOLDPEAK 320 temperature gun, -30-320°C). The inductively coupled plasma-

mass spectroscopy (ICP-MS) measurements were conducted with Agilent 7900 instrument for quantification of Cr-content. ^{1}H and ^{13}C1H NMR spectra were recorded using a Jeol JNM ECX 500 MHz spectrometer. HR-MS spectra were recorded on a Bruker Maxis Impact HD instrument. A programmable syringe pump (NE-300-ES, InfusionONE) from Darwin Microfluidics was used.

Synthesis of DAAQ-TFP COF:

DAAQ-TFP COF was synthesized via polycondensation between 2,6-diaminoanthraquinone (DAAQ) and 1,3,5-Triformylphloroglucinol (TFP).[18] In brief, DAAQ (68 mg, 0.284 mmol) and TFP (40 mg, 0.192 mmol) were taken in a Pyrex sealed tube (25 mL, 2 × 12.5 cm). The powders were properly mixed via a mechanical vortex shaker under dried condition for 5 min. To ensure an even dispersion of the reactants during the ongoing shaking process, N, N-dimethylacetamide (DMA, 1 mL) was added very quickly, followed by the addition of acetic acid (0.1 mL, 6 M). The reaction mixture was sealed with an airtight cap and heated at 120 °C for 2 days. After completion of the reaction, the dark brown colored precipitate was filtered off from the supernatant and washed several times using N, N-dimethylformamide (DMF). Finally, the precipitate was frozen at -80 °C and dried for two days by the lyophilization process.
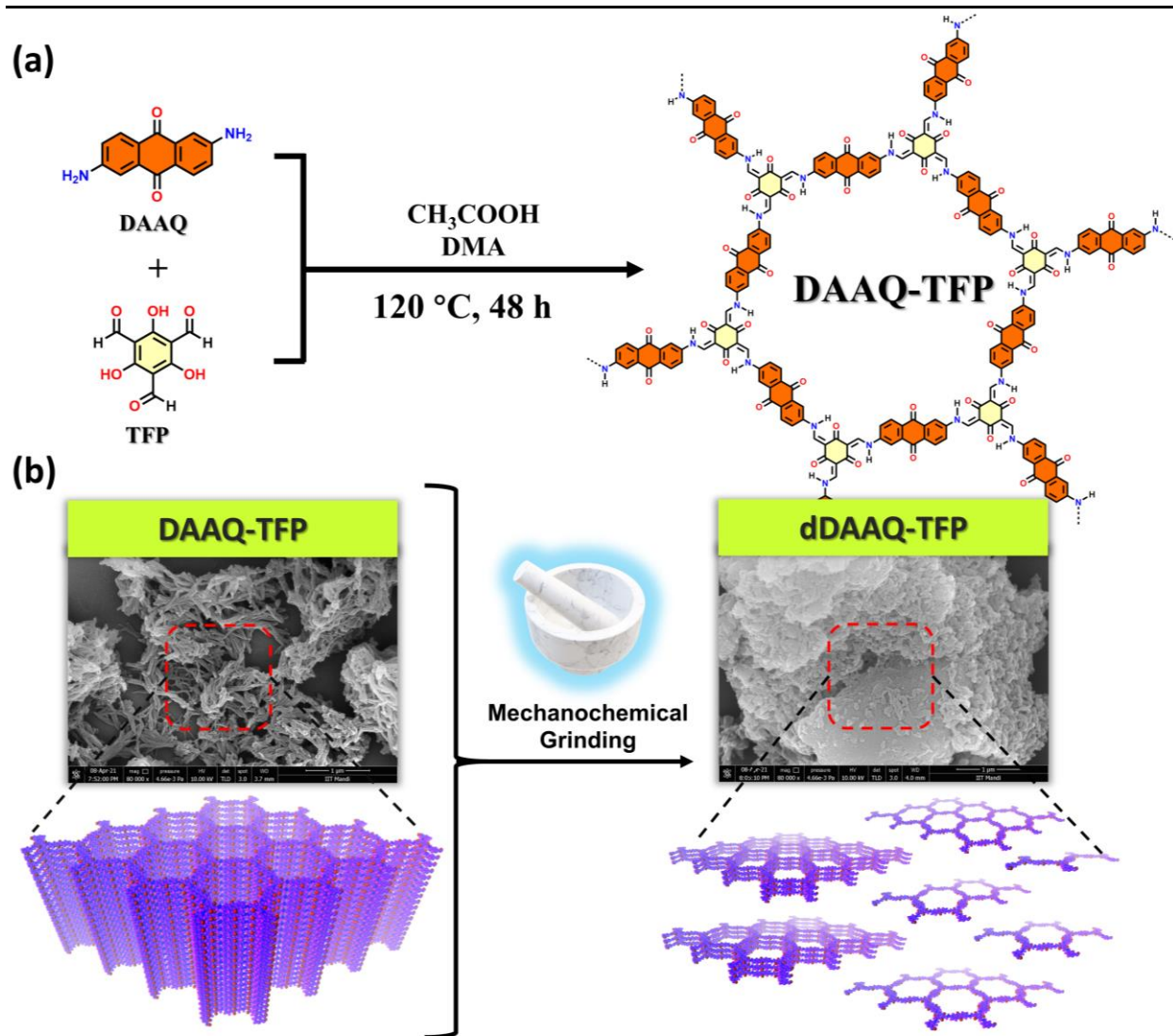
Synthesis of deformed DAAQ-TFP (dDAAQ-TFP):

Distortion in DAAQ-TFP was induced using a solvent assisted mechanical grinding process. Typically, the DAAQ-TFP COF (0.5 g) was taken in a clean agate mortar (8 cm × 6.5 cm × 1.8 cm). The material was consistently pulverized in a circular direction using a pestle. IPA (500 μL) was added to the material during the pulverization process over 90 min to prevent total drying. Lastly, the material was dried at 50 °C in a hot air oven. It was used directly for characterization and photocatalytic applications without any purification. The pulverized material will be labelled as dDAAQ-TFP in the article.

Photoelectrochemical Measurements

Transient photocurrent and electrochemical impedance spectroscopy (EIS) were measured using an Autolab electrochemical analyzer equipped with a standard three-electrode setup. Pt wire was used as the counter electrode and an Ag/AgCl (saturating KCl) electrode as the reference electrode. A 100 W visible light emitting LED was used as a source of illumination that was kept at a distance of 10 cm from the working electrode. The synthesised materials (5 mg) were thoroughly mixed with Nafion solution (5 wt%, 20 μL) and IPA-distilled water (480 μL) to create the ink. An F-doped SnO_2-coated glass (FTO glass) electrode (1.5 × 2.5 cm) with an active area of approximately 1.5 cm^2 was used to drop-cast the prepared ink. The transient photocurrent measurement was performed under an applied bias of 0.5 V. The EIS measurements were performed with an AC amplitude of 10 mV and a frequency range of 100 kHz to 0.1 Hz at a polarisation potential of 0.5 V. The electrolyte used in both studies was an aqueous solution of Na_2SO_4 (0.1 M).

Results and discussion

197 The DAAQ-TFP was synthesized via irreversible polycondensation reaction between TFP and
198 DAAQ according to the literature with some modifications.[18] Chemical structure of the COF is
199 depicted in **Scheme 1.** Deliberate mechanical pulverization was employed to tune the optical
200 property of the pristine COF. Extensive characterization of the dDAAQ-TFP was performed to
201 understand the change in physico-chemical properties of the material, as a consequence of the
202 mechanical grinding. A brick red colored DAAQ-TFP turned to dark red by extensive grinding of
203 90 min.

Scheme 1: (a) Schematic representation of DAAQ-TFP synthesis and (b) preparation of dDAAQ-TFP via post mechanical deformation of DAAQ-TFP.

204

205 Comparison of the FTIR spectra (**Figure 1a**) of the reactants and the COF revealed the formation
206 of the β-ketoenamine-linked DAAQ-TFP. This is evident from the appearance of the stretching
207 peaks at 1266 cm^{-1} (C-N) and ~3400 cm^{-1} (N-H).[19] DAAQ shows two characteristic stretching

208 peaks for primary amines (-NH$_2$) at 3500 and 3400 cm^{-1}. These peaks disappeared on COF
209 formation. Peak corresponding to CH=O stretching (2889 cm^{-1}) of the TFP also disappeared. The
210 mechanical pulverzation did not alter the chemical integrity of the COF as the FTIR spectrum of
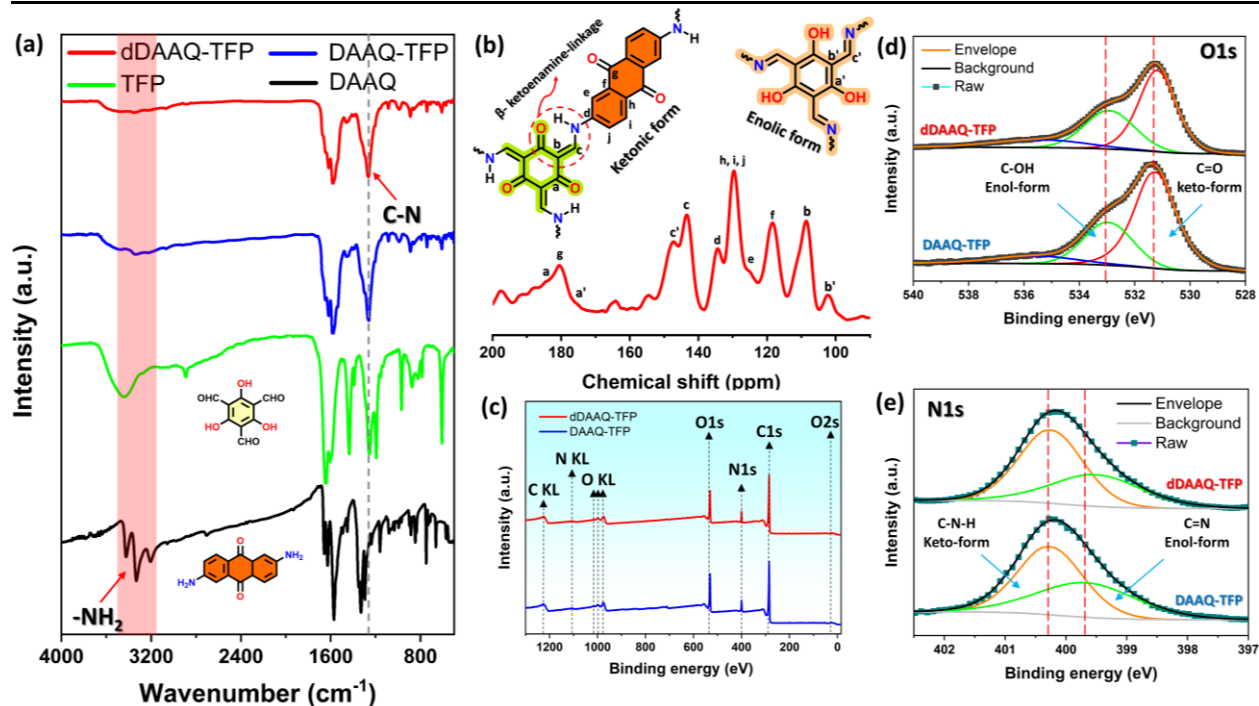211 dDAAQ-TFP was similar to the parent COF.[17]

Figure 1: Chemical structure analysis before and after mechanical grinding: (a) FTIR analysis, (b) β-ketoenamine linkage of dDAAQ-TFP confirmed via ^{13}C CP-MAS solid-state NMR spectrum, (c) XPS survey spectra and the narrow scan spectra of (d) O1s and (e) N1s.

212

213 Solid state ^{13}C CP-MAS NMR spectroscopy of dDAAQ-TFP was performed (**Figure 1b**). The
214 characteristic signals at 118 ppm (=CNH, α-enamine), 144 ppm (C*=CNH, β -enamine) and 181
215 ppm (C=O, carbonyl group) can be assigned to the presence of β-ketoenamine-linkage.
216 Additionally, we observed a characteristic resonance peak for C=O (180 ppm). This reveals that
217 the dDAAQ-TFP is constituted with anthraquinone-based building blocks in the framework.
218 Besides this, the NMR spectrum showed three minor signals at 102, 147 and 175 ppm because of
219 the coexistence of both enolic and ketonic forms of dDAAQ-TFP.[19,20]

220

221 XPS survey spectra of the pristine and grounded COF revealed the presence C1s, Ns and O1s as
222 shown in **Figure 1c**. Further, narrow scan spectra of O1s and N1s are shown in **Figure 1d and 1e**
223 respectively. N1s spectra showed two peaks at 400.2 eV (C-N-H) and 399.7 eV (C=N) respectively
224 corresponding to the keto and enol forms of DAAQ-TFP. Similarly, the O1s spectrum which
225 showed the corresponding peaks at 531.2 (C=O) and 533 eV (C-OH) respectively for keto and
226 enol forms.[19, 21] The functional groups remained the same after extensive grinding of DAAQ-TFP.
227 However, the keto form (C=O, 531.2 eV) in O1s and enol form (C=N, 399.7 eV) in N1s were

228 shifted to lower binding energies in DDAAQ-TFP. This may be due to the extension of bond
229 lengths specifically after post-grinding process (**Figure 1d, Figure 1e** and **Table S1**).
230 Solid state characteristics of the COF was assesses using pXRD pattern as shown in the **Figure 2a**.
231 Both the materials showed identical diffraction patterns. The peak at $2\theta \approx 3.4$ corresponding to the
232 (100) planes was observed as reported.[19] Additionally, a broad diffraction peak was observed in
233 the range of 5-15˚. The relative intensities and positions matched well with the staggered AB
234 stacking of the simulated pattern. The presence of a broad peak at $2\theta \approx 27.5$˚ further indicates the
235 layered structure of the COFs, which is due to the interlayer π-π stacking of the (001) planes.
236 Distance between the layers was calculated to be ~3.2 Å in DAAQ-TFP. However, the intensity
237 was moderately reduced and the peak shifted to $2\theta \approx 26.6$ after extensive grinding (see inset **Figure**
238 **2a**). Thus, grinding increases the inter-layer distance to ~3.4 Å. Moreover, changes in structural
239 aggregation and dislocation of layered structures are also expected due to the applied shearing
240 force.[22]

241 Both the DAAQ-TFP and dDAAQ-TFP showed type I reversible isotherms as shown in **Figure**
242 **2b**, attributed to their microporous frameworks. The correlation coefficients of each material
243 validate our experimental analysis (**Figure S2a** and **Figure S2b**). DAAQ-TFP and dDAAQ-TFP
244 COFs have BET surface areas of 552 and 265 m^2/g respectively. Both the microporous and external
245 areas (**Table S2)** as well as microporous volumes decreased due to grinding. As evident from the
246 pore size distribution plots (**Figure 2c** and **Figure 2d)** both the as synthesized and ground COF
247 have pore diameters mostly located between 1 and 1.6 nm respectively (see **Figure S3**). The
248 observed reduction in surface area as well as alteration of pore volumes could be ascribed to
249 shearing dislocations, folding, and deformations of 2D-layered structures as speculated in the
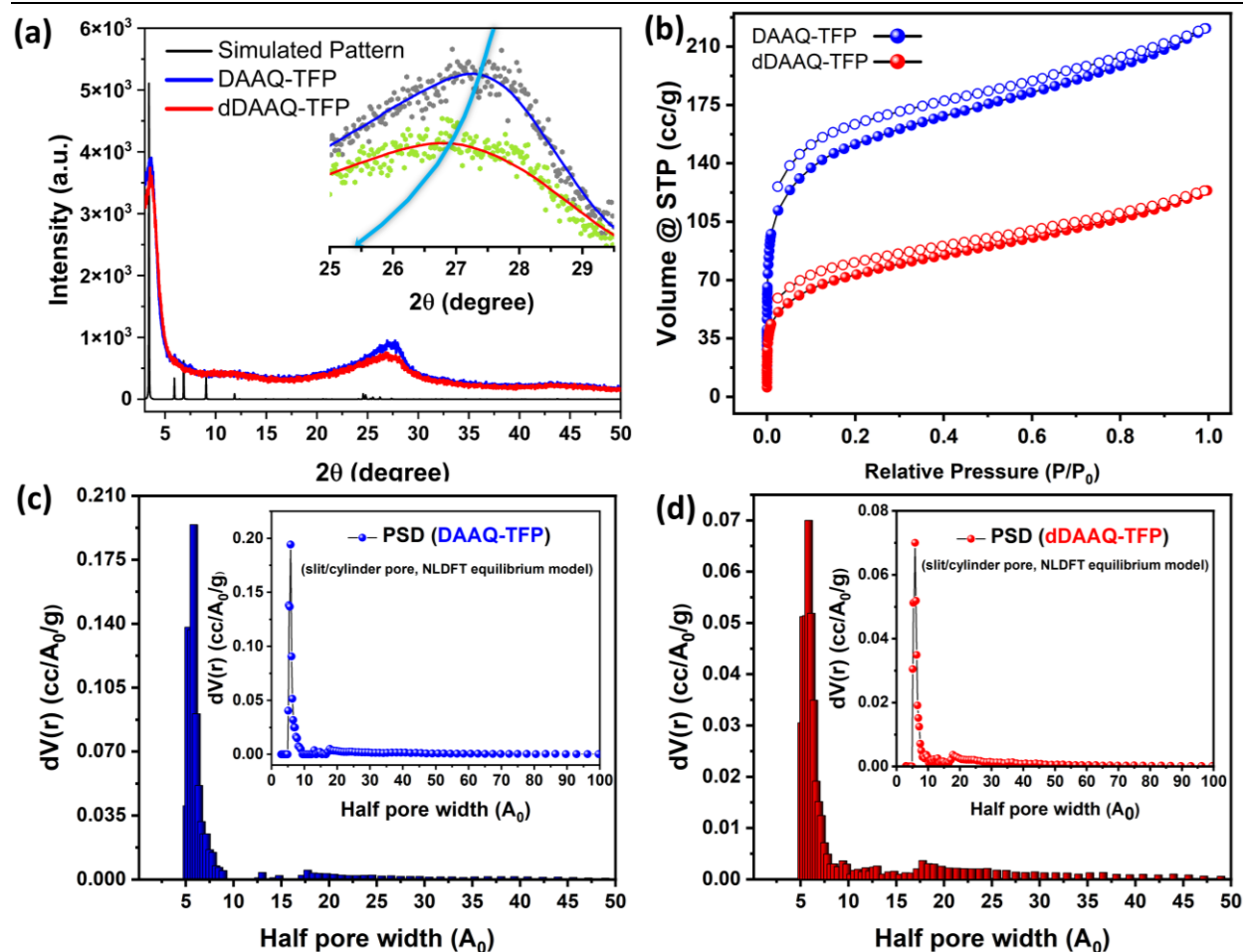250 literature.[22]

251

Figure 2: Comparison of (a) pXRD patterns and (b) adsorption-desorption isotherm of DAAQ-TFP and dDAAQ-TFP COFs via BET surface area analysis, BJH and NLDFT methods for pore size distribution of (c) DAAQ-TFP and (d) dDAAQ-TFP.

252

253 DAAQ-TFP COF particles possess nanofibrous morphology as shown in the **Figure 3,** which is
254 similar to the previous report.[19] Average diameter of the 1-D structures was found to be $\sim 72 \pm 32$
255 nm (**Figure S4**). However, the mechanical grinding led to the formation of 2D-flakes due to the
256 lateral fusion of fibres.[23] The fused aggregated structure of the nanofibers could be clearly
257 visualized using high resolution TEM (**Figure 3b** and **Figure 3e).**

258 Further, thermal stability of the DAAQ-TFP COF was slightly decreased on grinding. This was
259 evident from the early onset and completion of mass loss for DDAAQ-TFP than the pristine COF
260 (**Figure S5**). This could be the reduced interlayer interactions in dDAAQ-TFP than the rigid
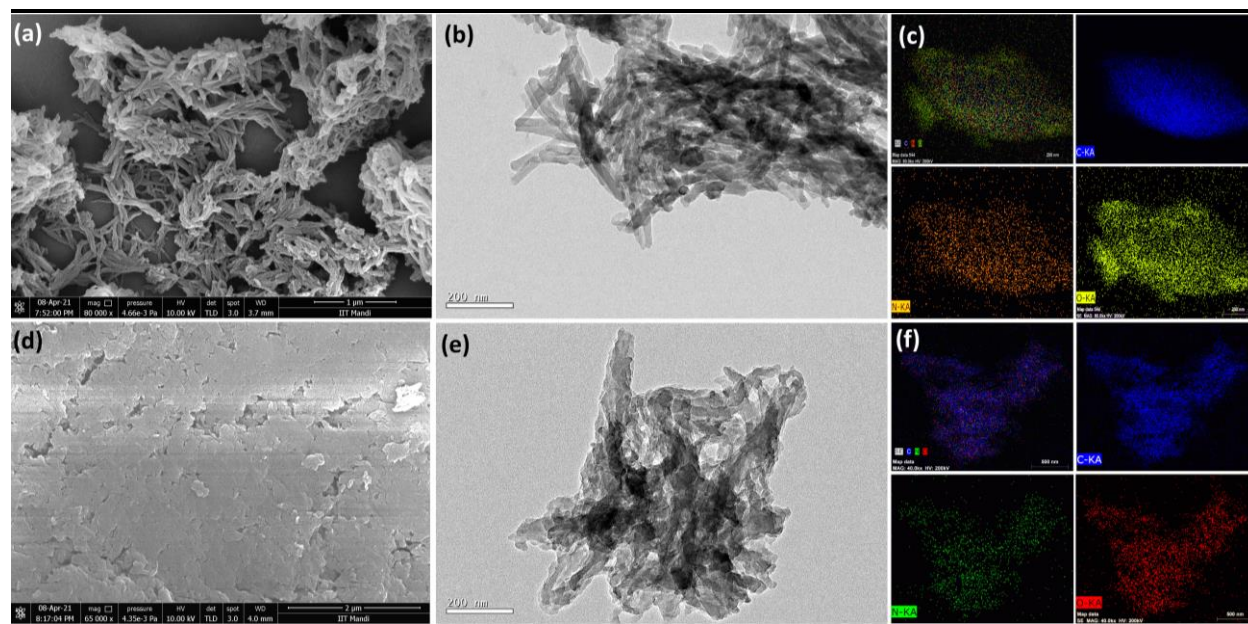261 DAAQ-TFP.

262

Figure 3: Particle morphology of DAAQ-TFP before and after PMD process: FESEM images of: (a) DAAQ-TFP & (b) dDAAQ-TFP, TEM images of (b) DAAQ-TFP & (e) dDAAQ-TFP and EDS-elemental mapping of: (c) DAAQ-TFP and (f) dDDAQ-TFP.

263

264 The pristine as well as grounded COF showed broad optical absorption ranging from UV to NIR
265 as shown in **Figure 4a** due to the extended π-conjugation. However, the λ_{max} of DAAQ-TFP at
266 ~505 nm shifted to ~480 nm on grinding. This could be due to the H-type aggregation of fibrous
267 structures that might have developed after mechanical grinding.[17] Alternatively, the formation of
268 2D structures due to grinding also can lead to hypochromic shift (25 nm) due to quantum
269 confinement. Similar findings were reported for g-C_3N_4.[24] The quantum confinement was also
270 evident from the reduced absorbance in the NIR region (645 - 1100 nm). Ultraviolet photoelectron
271 spectroscopy (UPS) survey spectra comparing the valence band maxima (VB) of the COFs are
272 shown in **Figure 4b**. Remarkably, the mechanical grinding induced dramatic change in VB
273 positions. DAAQ-TFP shows VB at +1.1 eV (vs E_f) that was significantly reduced to +0.8 eV (vs
274 E_f) for the identical kinetic energy cut off value of 16.4 eV (right inset **Figure 4b**).
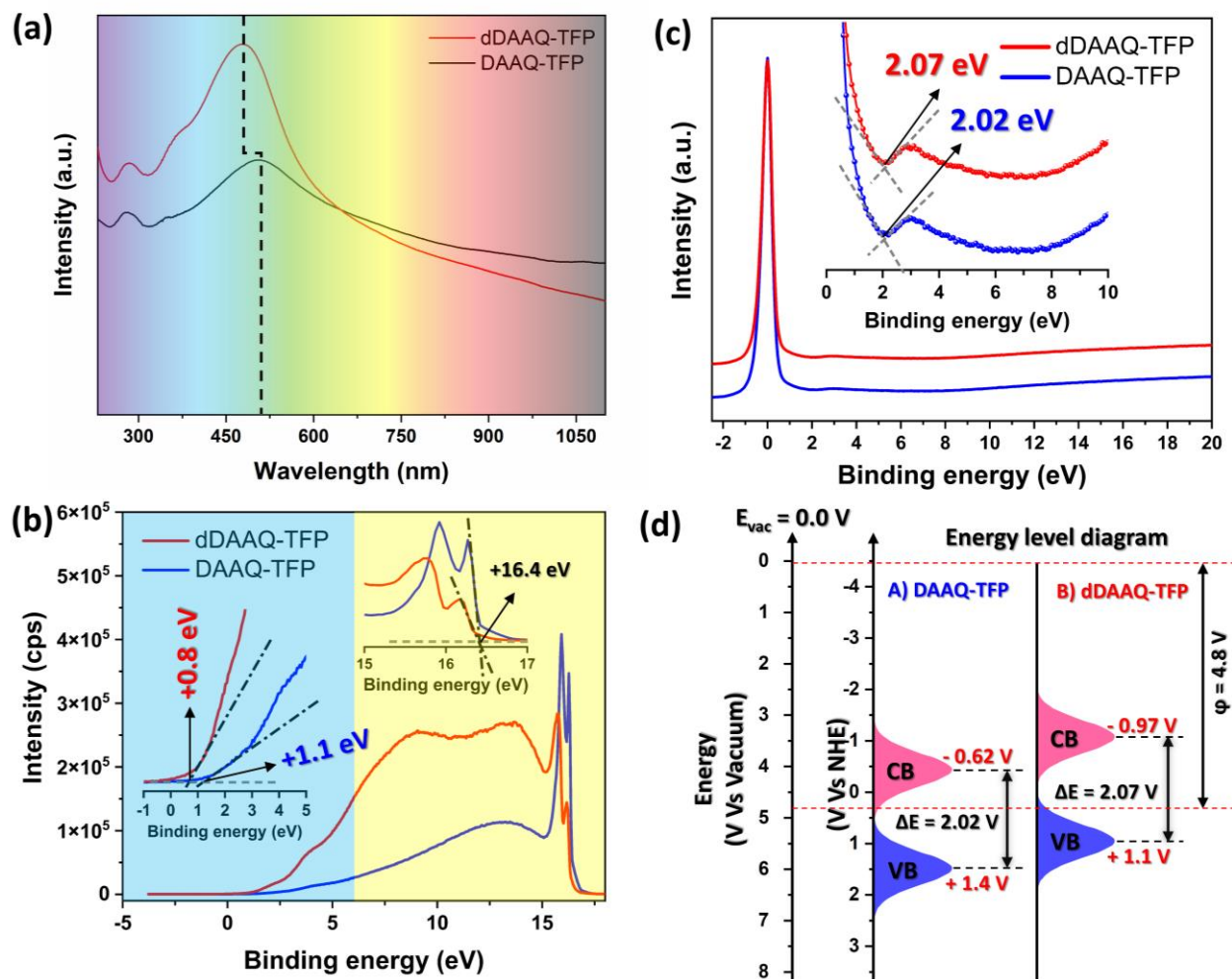
Figure 4: Energy diagram for DAAQ-TFP and dDAAQ-TFP: (a) UPS spectra, (b) REEL spectra and (c) schematic representation of energy level diagram comparing the effect of PMD process obtained from UPS and REELs measurements.

275

Figure 4c shows a typical reflected electron energy loss spectrum (REELS) of the materials to investigate the absolute surface band gaps of the materials.[25] The dominant peaks due to elastically scattered electrons (Rayleigh line) and the inelastically scattered electrons appeared in the spectra. Onset value of the Rayleigh line determines the photoelectrical band gap. Thus, the band gap for DAAQ-TFP and dDAAQ-TFP was found to be 2.02 and 2.07 eV respectively. The band gap increment on mechanical grinding, through very minimal, signifies the hypochromic shift that was observed in the absorbance spectra. The conduction band (CB) minima for both the materials were calculated using the empirical formula: $CB = VB - \Delta E$.[21] The calculated CB for DAAQ-TFP and dDAAQ-TFP were found to be -0.62 and -0.97 (eV vs E_f) respectively. The band positions were also determined with respect to vacuum vs NHE (0 V vs NHE is equivalent to -4.5 eV vs vacuum).[26] The band positions\ are summarized in the **Table S3** and the **Figure 4d**. The results for DAAQ-TFP closely matched with the previous literature.[19]
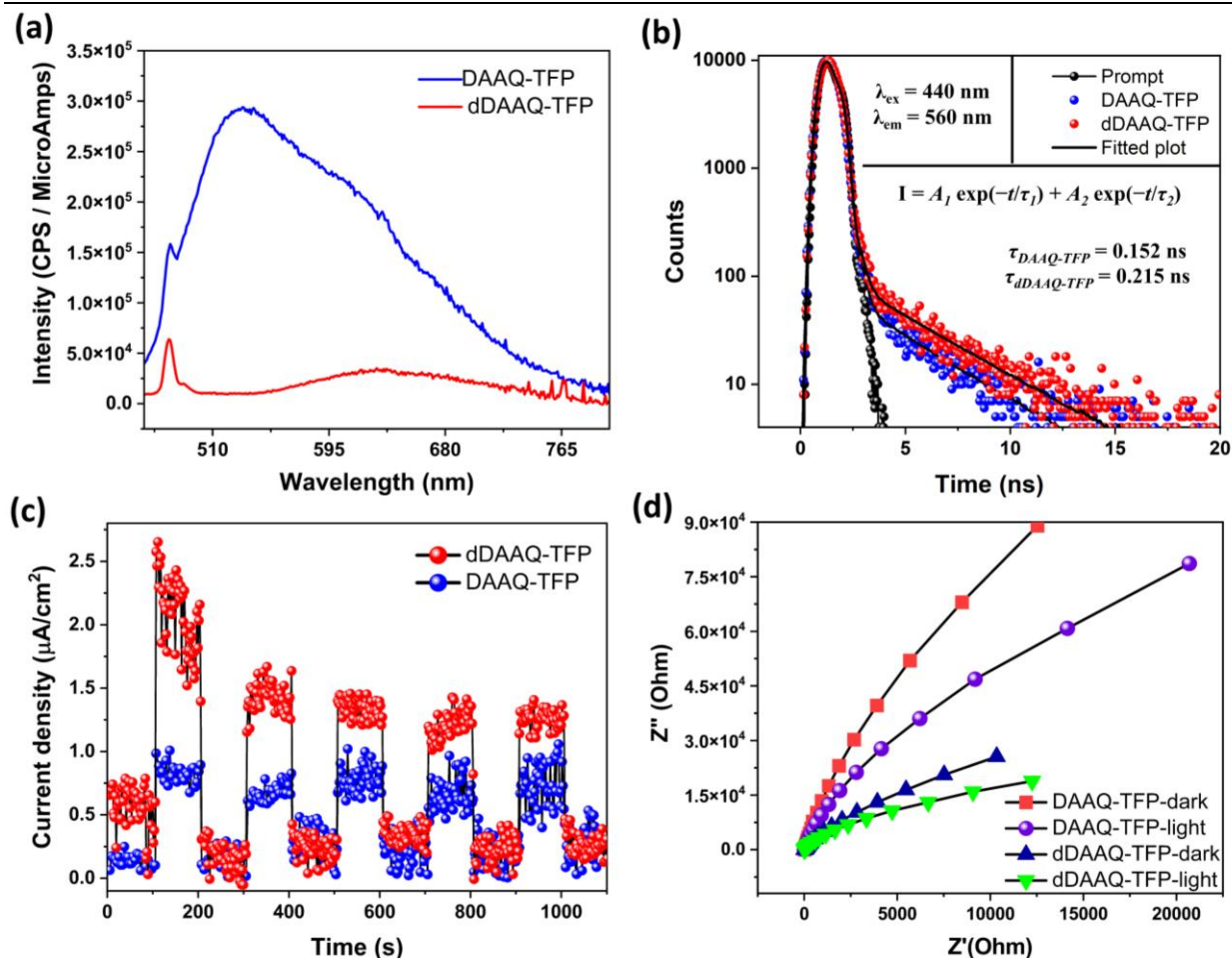
Figure 5: photo- and photoelectrochemical properties of DAAQ-TFP and dDAAQ-TFP: (a) PL spectra, (b) Lifetime measurement, (c) photocurrent measurement, (d) Nyquist plot for EIS spectra.

288

Photoluminescence spectra:

290 The ability to generate electrons and holes on exposure to light is the characteristic property of any
291 photocatalyst. One of the key reasons for lowered efficiency of photocatalysts is the recombination
292 of electrons and holes to excitons (bounded electron-hole). The recombination is associated with
293 intense photoluminescence (PL). Therefore, steady state PL spectra were acquired to evaluate the
294 stability of the photogenerated charges from the material and shown in **Figure 5a**. The DAAQ-
295 TFP showed broad and intense emission spectrum at ~530 nm. In contrast, the PL intensity is
296 significantly reduced for dDAAQ -TFP. This implies that the dDAAQ-TFP produces stable
297 electrons and holes than DAAQ-TFP.[27] Furthermore, dDAAQ-TFP showed red shifted emission
298 spectra by ~102 nm which possibly is due to the molecular aggregation as evident from the
299 electron micrographs (**Figure 3b** and **Figure 3e**). The blue shift in absorbance spectrum and
300 corresponding red shift in the PL spectrum confirms the H-type aggregation of COF fibres on
301 grinding.[17] A relatively narrow peak was also observed at lower wavelength region (~478 nm)

302 corresponding to the water Raman scattering due to the molecular valence vibration of -OH
303 functional group.[28]

304 To validate improved electron-hole separation efficiency, the relaxation pathways of the
305 photoexcited electrons were probed using time resolved emission spectroscopy (TRES). The
306 lifetime decay profiles were fitted with bi-exponential function for both materials indicating two
307 types of relaxation process of the excited electrons (**Figure 5b**). Initially, the average lifetime of
308 as prepared DAAQ-TFP was 0.152 ns which was increased to 0.210 ns after mechanical
309 aggregation process. This undoubtedly indicates the ground COF provides enhanced electron-hole
310 pair stability than DAAQ-TFP.[29]

311 Further, a transient photocurrent response of the DAAQ-TFP and dDAAQ-TFP materials was
312 measured over several on-off irradiation cycles to assess the effectiveness of electron-hole
313 separation. It is evident from the **Figure 5c** that the current density of the ground material is
314 significantly higher than the pristine COF. Evidently, the dDAAQ-TFP showed better photocurrent
315 responses than the DAAQ-TFP implying the generation of more charges on exposure to light.

316 The carrier charge dynamics of the materials were verified via the electrochemical impedance
317 spectroscopy (EIS) in a three-electrode cell system. DAAQ-TFP and dDAAQ-TFP exhibited
318 semicircular Nyquist plots as shown in the **Figure 5d**. dDAAQ-TFP exhibited an excellent reduced
319 resistance than DAAQ-TFP irrespective of the dark or light conditions. This further clarifies a
320 sluggish relaxation of charge carriers via self-recombination process in case of dDAAQ-TFP than
321 DAAQ-TFP.

322 **Photocatalytic activities of COF materials:**

323 **a) Photocatalytic reduction of hexavalent chromium:**

324 Chromium is a lustrous metal that resists chemicals from corrosion and thus provides a lifetime
325 durability in a variety of daily used commodities (e.g., stainless steel, leather tanning, photographic,
326 etc.). Due to their increased use, industrial discharge of hexavalent chromium (Cr^{6+}) into the
327 environment is a great concern. Cr^{6+} is toxic, mutagenic, and carcinogenic and it can easily enter
328 the food chain.[30] The recommended permissible limit for Cr^{6+} in drinking water is 0.05 ppm.[31]
329 Several strategies are being employed to eliminate Cr^{6+}, including reduction to Cr^{3+}, which is many
330 folds lees toxic than Cr^{6+}.[32] Furthermore, Cr (OH)$_3$ is a solid precipitate which can easily be
331 removed from water.[33] In fact, trace amounts of Cr^{3+} is an essential mineral for human diet.[34] To
332 validate our observations, the COF materials were applied for photocatalytic reduction toxic
333 chromium (Cr^{6+}) as anthropogenic pollutants. The removal of Cr^{6+} concentration was
334 calorimetrically determined using 1,5-diphenyl carbazide (DPC) method. In acidic medium, Cr^{6+}
335 oxidizes DPC to 1,5-diphenylcarbazone (DPCA) resulting a purple colored Cr^{3+}-DPCA complex
336 with maximum absorbance at $\lambda_{max} = 540$ nm (**Eq. 1**).[35] Thus, the decrement of the absorption peak
337 over time was assessed for the evaluation of Cr^{6+} removal.

$$Cr^{6+} + Colorless\ DPC\ +\ Acid \rightarrow purple\ Cr^{3+} - DPCA\ complex \qquad \text{Eq. 1}$$
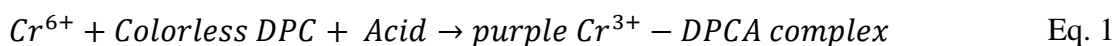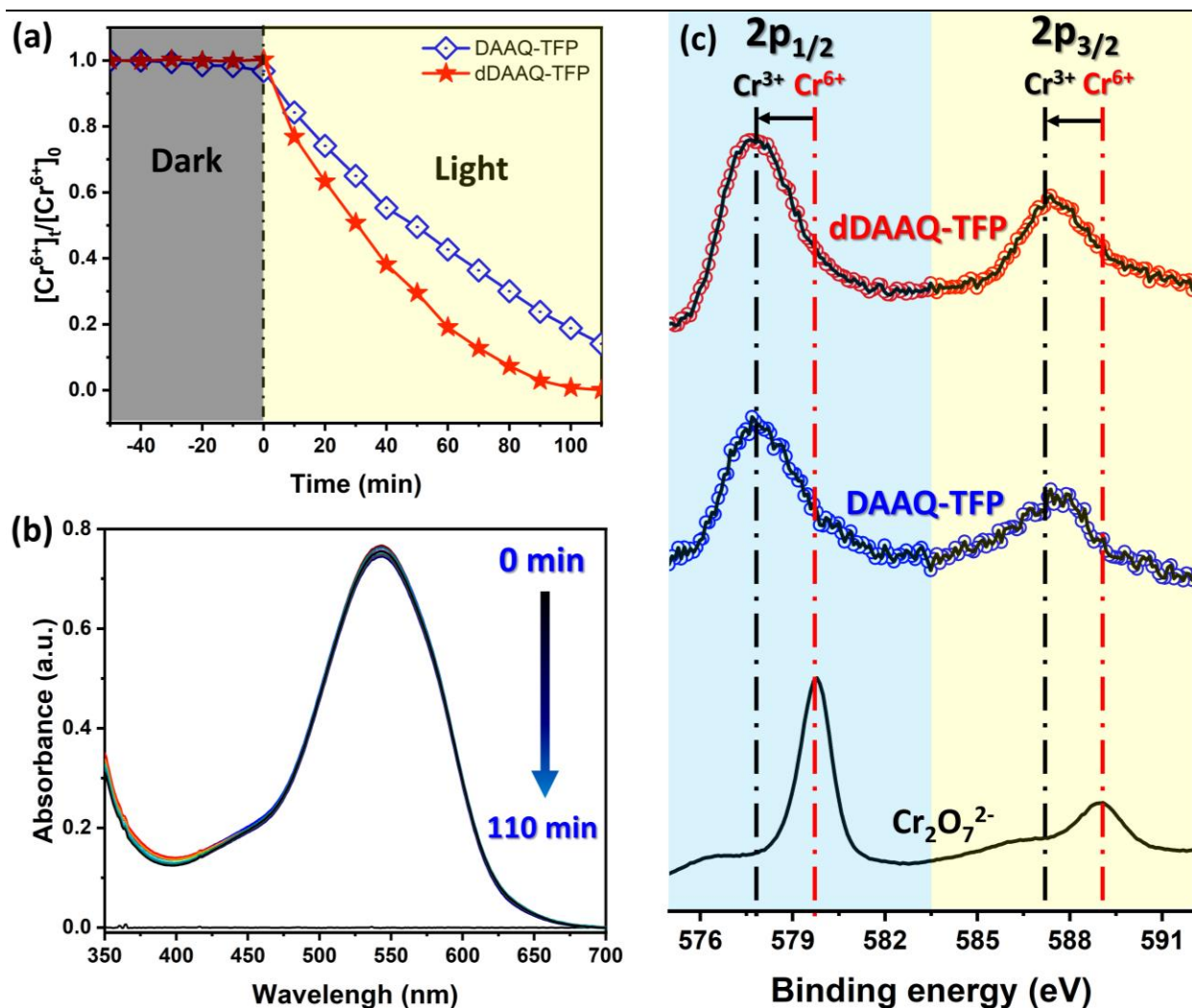
Figure 6: (a) Photocatalytic reduction of Cr^{6+} using DAAQ-TFP and dDAAQ-TFP; (b) reduction in absence of photocatalyst and, (c) XPS analysis of $Cr_2O_7^{2-}$ (before) and Cr^{3+} after photocatalytic reduction using dDAAQ-TFP (top) and DAAQ-TFP (middle) under white LED. Reaction condition: $[Cr^{6+}] = 30$ ppm, $[dDAAQ\text{-}TFP] = 0.1667$ mg mL^{-1}, white light, pH = 3, and T = RT.

339

340 Initially, COF materials in Cr^{6+} solution was stirred under in dark to achieve adsorption-desorption
341 equilibrium (**Figure 6a**). Cr^{6+} is barely adsorbed by the COF materials under dark conditions. Even
342 after 50 minutes, only ~3% of Cr^{6+} is adsorbed in case of DAAQ-TFP while dDAAQ-TFP did not
343 show any noticeable sorption. DAAQ-TFP is constructed with ordered porosity assembled by π-
344 π^* stacking of hexagonal layered structures. Therefore, a relatively higher adsorption was observed
345 that could be due to the higher BET surface area as discussed earlier (**Figure 2b-d**). As evident
346 from the XRD analysis, the PMD of DAAQ-TFP the porous cylindrical alignment of DAAQ-TFP
347 affected sorption of Cr^{6+}. After the saturated adsorption-desorption equilibrium, the reaction

348 mixture was exposed to visible light. A comparative Cr^{6+} reduction efficiency was evaluated using
349 the empirical relation below (**Eq. 2**):[36]

$$Photocatalytic\ efficiecny\ (\%) = \left(\frac{C_0 - C_t}{C_0}\right) \times 100\% \qquad\text{Eq. 2}$$

350 Remarkably, dDAAQ-TFP was able to reduce more than 96% of Cr^{6+} in 90 minutes. While DAAQ
351 showed almost complete reduction in 210 minutes as shown in **Figure 6a**. Inset showing typical
352 discoloration of the pink Cr^{3+}-DPCA complex. It is worthy to mention that no evidence of
353 reduction was observed in absence of the photocatalysts (**Figure 6b**). This indicates the
354 photoreduction is only induced in presence of photocatalysts. Nevertheless, dDAAQ-TFP gains an
355 advantage over time in the reduction of Cr^{6+}. This could be fact that the mechanical grinding of
356 DAAQ-TFP also enhances photoreduction ability. It is evident that reducing Cr^{6+} produces lower
357 oxidation states for Cr-species. The reduction of Cr^{6+} to Cr^{3+} requires a potential of 1.33 V vs
358 NHE.[32,37] After complete reduction, the catalysts were separated via centrifugation of reaction
359 mixture from the reaction mixture. XPS analysis was performed immediately after completion of
360 the reaction (**Figure 6c**. Typically, Cr^{6+} shows two characteristic signals at 579.8 and 589 eV
361 which corresponds to spin-orbit coupling for $2p_{3/2}$ and $2p_{1/2}$ respectively. Interestingly upon
362 photoreduction process, the signals were significantly shifted to lower binding energy positions
363 (577.7 and 587.3 eV). This result implies the effective photoreduction Cr^{6+} under visible light
364 irradiation.[36] The Photocatalytic reduction of hexavalent chromium is compared with the literature
365 which clarifies a comparable photocatalytic activity as shown in the **Table 1**.

Table 1: Comparison for visible light active photocatalysts for reduction of hexavalent chromium.

Sl. No.	Photocatalysts	$[Cr^{6+}]$ (mg L^{-1})	[Catalyst] (mg mL^{-1})	Source	Time (min)	Efficiency (%)	Year
1.	TPB-BT-COF*	10	1	Xe lamp (> 400 nm)	75	99	2019[32]
2.	TAPT-BT-COF*	10	1	Xe lamp (> 400 nm)	105	80	2019[32]
3.	P-FL-BT-3*	25		1.2 W/cm^2	120	100	2015[38]
4.	g-C$_3$N$_4$#	10		-	180	50	2017[39]
5.	Py-SO$_1$#	10	0.1	300 W(> 420 nm)	90	93	2022[40]
6.	Poly (Triazine Imide)	10	0.2	Xe lamp (>400 nm) 300 W	120	44	2019[41]
7.	NC350#	50					
8.	(SCN)n polymer (2.0)#	10	2	LED (300 W, 420 nm)	120	~98	2020[42]
9.	RP-AP-0.5#	60	1	350 W, >420 nm	120	>98	2021[43]
10.	BUC-21/g-C$_3$N$_4$ (B100G100)#	10	0.25	Xe lamp (500 W, >420 nm)	120	100	2018[44]

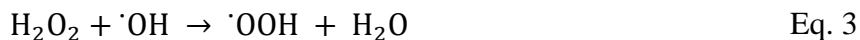|							
11.	BUC-21	10	0.25	Xe lamp (500 W, >420 nm)	120	13	2018[44]
12.	Siloxene sheets	10	0.1	-	60	>99	2021[45]
13.	dDAAQ-TFP#			LED (100 W, >400 nm)			**This work**

[*]Inert atmosphere.
[#]Acidic pH.

366

b) Photo-Fenton like reactions:

368 Industrialization led to production of the various complex pollutant day by days. It needs cutting-
369 edge technologies to protect the drinkable water from these types of pollution. Fenton-reactions
370 are traditionally used as advanced oxidation process for decontamination of pollutants. Owing to
371 the exceptional aqueous stability, semiconductivity, heterogeneity, and high reactivity, we
372 carefully examined for Fenton-like degradation of organic pollutants. Accordingly, the materials
373 were further employed for photo Fenton-like activities under visible light. The photoactivation of
374 peroxide was evaluated by considering methyl orange (MO) as a model organic pollutant. To
375 determine the adsorption capacities of COF materials, equilibrium adsorption-desorption
376 experiments were conducted in dark. After 60 minutes of stirring, equilibrium was reached.
377 Despite of exceptionally high surface area, the materials are mediocre for the MO adsorption (only
378 <2%). The inferior sorption of the materials can be ascribed to the identical surface charges of the
379 materials as of MO (an anionic organic pollutant) as evident from the zeta potential experiment.
380 Further, the porosity of the sorbent materials affects the sorption behaviour as well as the size of
381 the molecules adsorbed. Based on the BET pore diameter analysis, COF materials have narrower
382 pores that cannot accommodate larger MO molecules (ca. $1.31 \times 0.55 \times 0.18$ nm).[46] After
383 adsorption saturation, the reaction was continuously stirred under a source of visible light
384 illumination. Decrement of MO concentration is alternatively representing the generation of highly
385 reactive oxygen species (ROS). After 240 minutes of irradiation, the removal efficiency of the
386 DAAQ-TFP was only ~24% while ~84% for dDAAQ-TFP (**Figure S7**). The photocatalytic
387 degradation results were well fitted with pseudo first-order kinetics (**Figure S8**). DAAQ-TFP
388 showed an apparent rate constant value (k) of 8.20×10^{-4} min^{-1} which is significantly improved to
389 7.85×10^{-3} min^{-1} upon mechanically grinding process. The degradation ability of dDAAQ-TFP is
390 ~9.5 times higher than the DAAQ-TFP. For an ideal Fenton or Fenton-like reactions, the ability
391 of degradation of analysts is much improved when H_2O_2 like agent are added to the reaction system.
392 In fact, such catalysts produce highly reactive oxygen species (ROS) via activating less/non-
393 reactive species (here, H_2O_2). Therefore, to examine the ability to activate H_2O_2, the degradation
394 was further evaluated by varying the H_2O_2 concentrations from 0.15 to 0.9 M at the identical
395 parameters. As expected, the removal efficiencies were significantly accelerated after addition of
396 H_2O_2. It is evident from the **Figure S9** that the removal efficiencies were boosted to ~42% and
397 ~70% respectively for DAAQ-TFP and dDAAQ-TFP only in 30 minutes. Further increasing the
398 concentration of H_2O_2 is also greatly enhanced the removal efficiencies. In particular, DAAQ-TFP

and dDAAQ-TFP showed a maximum of ~85% and ~95.4% of removal efficiencies respectively at the higher H_2O_2 concentration (0.9 M). It could be observed that the dDAAQ-TFP outperformed higher removal efficiency than DAAQ-TFP even at lower concentrations of H_2O_2. The slow increment of removal efficiency at the expense of higher H_2O_2 amount is probably due to the self-scavenging of ·OH radicals as expressed by the equations (**Eq. 3** and **Eq. 4**).[5,6] The evidence of ·OH production is discussed further in the later section.

$$H_2O_2 + {}^{\cdot}OH \rightarrow {}^{\cdot}OOH + H_2O \qquad\qquad \text{Eq. 3}$$
$$^{\cdot}OOH + {}^{\cdot}OH \rightarrow H_2O + O_2 \qquad\qquad \text{Eq. 4}$$

H_2O_2 slowly undergoes photolysis when exposed to light especially lower wavelengths ($\lambda < 400$ nm).[37] To validate the photocatalytic activities that outstripped by the photocatalysts, we performed the reactions in the absence of photocatalysts. Remarkably, only 3.5% efficiency was observed in dark which was accelerated to 17% after light illumination for 30 minutes (**Figure S10**). The results undeniably confirm the Fenton-like reactions predominantly due to the photocatalysts.
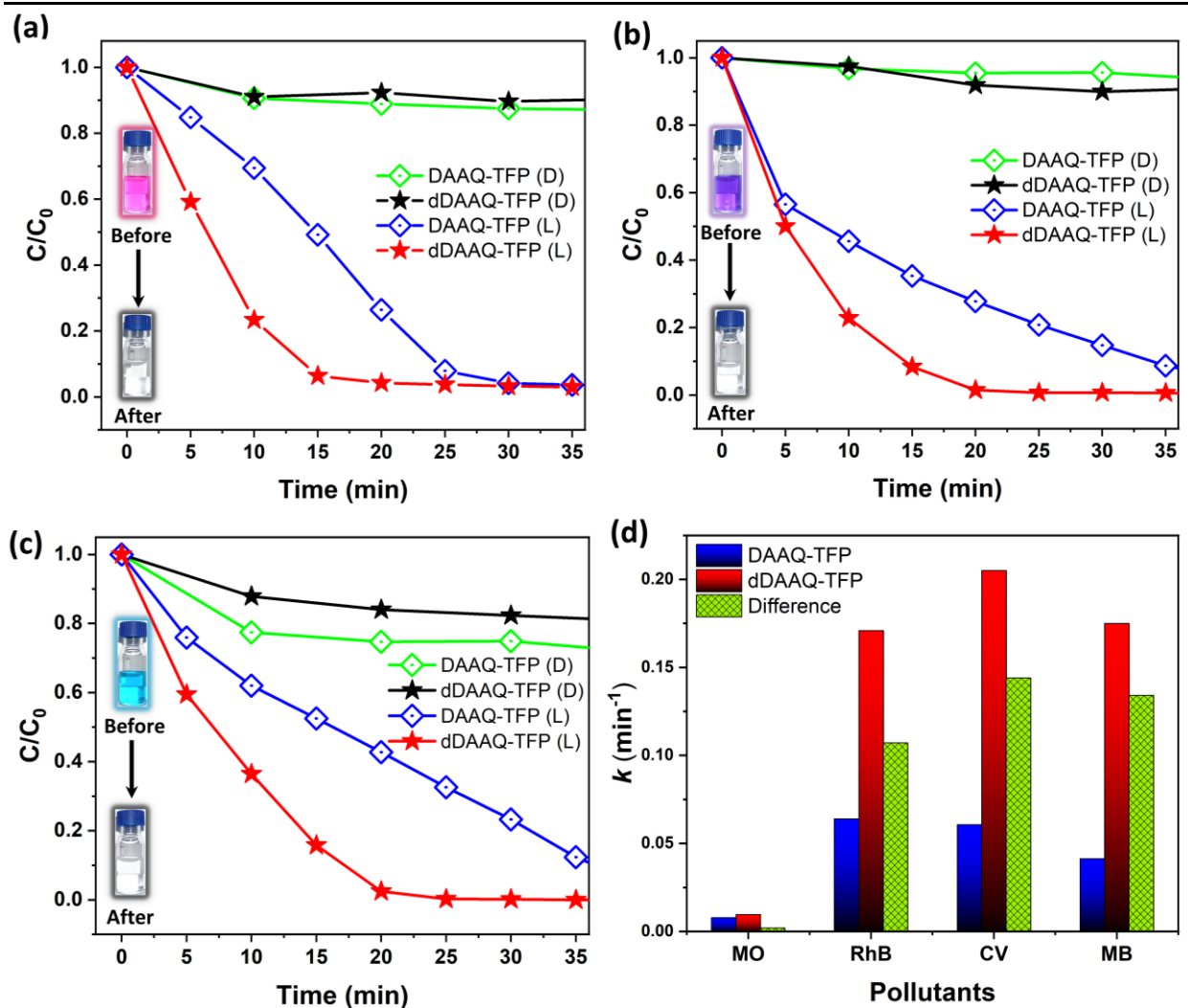
Figure 7: Photocatalytic Fenton-like reaction for various organic pollutants. (a) RhB, (b) CV, (c) MB and (d) activities of DAAQ-TFP and dDAAQ-TFP for various organic pollutants. Reaction conditions: [Pollutant] = 98.2 ppm, $[H_2O_2]$ = 0.15 M, photocatalyst = 0.1 g L^{-1}, white LED and T = RT.

411 It is essential to optimize the amount of photocatalysts used in a Fenton-like degradation process
412 to ensure the process is economically viable. Accordingly, the Fenton-like reaction was performed
413 at three different concentrations of dDAAQ-TFP i.e., 0, 0.1, 0.3 and 0.5 g L^{-1}. The higher amount
414 of dDAAQ-TFP exponentially increases the MO removal efficiencies. A photocatalyst
415 concentration of 0.1 g L^{-1} is sufficient to degrade MO considerably in a very short period (**Figure**
416 **S10).** A reduction of ~19% MO in 60 minutes was enriched to 79% with only 0.1 g L^{-1} dDAAQ-
417 TFP. This clearly indicates the photocatalyst plays an essential part of the Fenton-like reactions.
418 Concentration of catalysts usually increases reaction rate due to the availability of active sites.
419 Nevertheless, the higher concentration of a photocatalyst sometimes educes reaction rate due to
420 the scattering dominant phenomenon rather than light absorption.[47,48] As a result, we have observed
421 saturated removal abilities at higher catalyst amounts (**Figure S11**). Alternatively, this validates
422 the Fenton-like degradation is considerably economic at lower concentrations of the photocatalyst.

423 To examine the broad range applicability, DAAQ-TFP and dDAAQ-TFP both were employed for
424 removal of several other common cationic organic pollutants. This includes, rhodamine B (RhB),
425 crystal violet (CV) and methylene blue (MB). As displayed in the **Figure 7**, the photocatalytic
426 Fenton-like degradation showed highly appealing results for the cationic the organic pollutants. In
427 fact, a small-scale amount of dDAAQ-TFP (0.1 gL^{-1}). Additionally, only 0.15 M H_2O_2 were
428 required to accomplish the nearly complete degradation of the pollutants. For instance, we could
429 achieve 96%, 99% and 98% removal efficiencies for RhB, CV and MB respectively which is just
430 in 20 minutes of visible light irradiation. In contrast, the resulting degradation completion for
431 DAAQ-TFP were only 74%, 72% and 57% respectively. The rate for degradation of dDAAQ-TFP
432 is much improved that could be seen from the **Figure 7**. Furthermore, the curves were fitted using
433 pseudo-first-kinetic curve fitting model by plotting -$\ln(C/C_0)$ vs. t and their corresponding fitted
434 plots are shown in **Figure S12**, **Figure S13** and **Figure S14** respectively for RhB, CV and MB.
435 The apparent rate constants (k) of DAAQ-TFP for the various pollutants were obtained which are
436 6.41×10^{-2} min^{-1}, 6.07×10^{-2} min^{-1} and 4.14×10^{-2} min^{-1}. In case of dDAAQ-TFP, the k values are
437 significantly boosted to 1.71×10^{-1} min^{-1}, 2.05×10^{-1} min^{-1} and 1.75×10^{-1} min^{-1} respectively. The
438 differences in k values could be easily assessed from the **Figure 7d**. On the other hand, the
439 performances are considerably reduced for MO (**Figure S15**) under the similar reaction conditions.
440 This may be due to identical molecular charge of MO as the COF materials as evident from the
441 zeta potential of materials. Despite of being less removal efficiency towards MO, still dDAAQ-
442 TFP showed photocatalytic activity ($k = 1.82 \times 10^{-3}$ min^{-1}) than the DAAQ-TFP under identical
443 reaction conditions (**Figure S16**). The removal efficiency of dDAAQ-TFP for MO, RhB, CV and
444 MB are 1.23, 2.67, 3.38 and 4.23 times improved as compared to DAAQ-TFP. The contributions
445 of light over total degradation of the pollutants are also evaluated after 20 minutes of reaction by
446 using **Eq. 2**. It is evident from the **Figure S17** that the light contribution (%) are considerably
447 higher in case of dDAAQ-TFP than DAAQ-TFP. This evidence is proving the improved

448   photocatalytic ability after grinding process. The increasing order of visible light utilization for
449   various pollutants is arranged as MO < MB < RhB < CV.

Impact of light towards photocatalytic reactions:

451   To ensure the influence of visible light, the photocatalytic reactions were evaluated via several
452   experimental analysis. Firstly, the photo Fenton-like degradation of MB was evaluated via 'on-off'
453   experiment. Typically, the visible light was switched intermittently after 5 min intervals during
454   the reaction. It could be seen that the reaction rate is nearly unchanged when the light was turned
455   off. Surprisingly, a dramatic increase in reaction rate was observed immediately under the light on
456   conditions. This clearly indicates the photocatalytic activity of dDAAQ-TFP is significantly
457   influenced by visible light. In addition, DAAQ-TFP is still able to remove MB despite that the
458   shoddier removal efficiency than dDAAQ-TFP. Eventually by mechanically grinding COF, the
459   photo Fenton-like reaction can be greatly enhanced. The experimental results are represented in
460   the **Figure 8a**.

461   For an ideal photocatalytic system, intensity of light is directly reliant to reaction rate. Thus, the
462   relationship between the intensity of visible light and photocatalytic activity was further illustrated.
463   The analysis was carried out using varied intensities of 0, 0.8, 2, 12, and 18.4 mW cm^{-2} while
464   maintaining the other parameters constant. The removal efficiencies of MB exhibit a direct
465   dependence on intensities, as seen in **Figure 8b**. After irradiation for 25 minutes, the measured
466   efficiencies of were found to be 6.27, 22.4, 73, 93.5 and 98.65% for 0, 0.8, 2, 12, and 18.4 mW
467   cm^{-2} respectively. This is primarily caused by the larger number of photons absorbed at increasing
468   light intensities.[47,49] Initially, the efficiency was rapidly enhanced up to 2 mW cm^{-2} whereas a
469   slower reaction rate is evident as the intensity increased further. The steady increment in
470   degradation efficiency may be caused by the formation of more ˙OH species by the dissociation of
471   H_2O_2, which are likely self-scavengers at higher intensities as discussed earlier (**Eq. 3** and **Eq 4**).

472   In order to assess the effectiveness of the photocatalyst, apparent quantum yield (AQY) was
473   evaluated. It measures the number of effective photons required for photocatalytic reaction.
474   Therefore, AQYs were determined via exciting the photocatalyst at three different monochromatic
475   lights. For instance, we considered 454 (blue), 515 (green) and 629 nm (red) for the photo Fenton-
476   like degradation of MB. **Figure 8c** shows a typical setup for a photocatalytic reaction equipped
477   with monochromatic LED source. According to the mathematical relation (**Eq. S3**), the AQY
478   values were calculated for the three wavelengths. We are highly amused to report that the dDAAQ-
479   TFP showed very high AQYs under identical reaction conditions. For λ_{max} = 454 nm, a highest
480   AQY of 41.01 ± 1.36% which indicates the photocatalyst is highly active for solar light utilization.
481   Evidently, the lower wavelengths of incident light exhibited higher AQYs as shown in the **Figure**
482   **8c**. The excitation of 515 and 629 nm, the AQYs are found to be 32.87 ± 0.52 and 8.80 ± 1.41
483   respectively (**Table S4**). There is no uncertainty that the dDAAQ-TFP absorbs the most lights in
484   the shorter wavelengths and thus a larger amount of charge carriers is produced for the faster
485   reaction rate. Further, the action spectrum was plotted in order to draw a correlation wavelength

486 dependent efficiency of the photocatalyst. The action spectrum can be obtained by one-to-one
487 mapping of AQY over the absorbance spectrum of the photocatalyst.[47] As shown in **Figure 8c**, the
488 results show that the photocatalyst is truly dependent on visible light which are reasonably
489 appealing. Additionally, we have calculated the photocatalytic space time yield (PSTY).[50] To
490 maintain the process's environmental impact to a minimal level, PSTY implies that the energy
491 needed to light the lamp should be reduced (see **Eq. S4** and **Eq. S5**). The PSTY values obtained
492 at various stimulated wavelengths are well correlated with the AQY values as summarized in
493 **Table S4**.

494 A photocatalytic reaction rate is influenced by a variety of operational parameters. This includes
495 concentrations of pollutant, photocatalyst, peroxide, lighting source power, and reaction duration
496 over conversion efficiency. Exclusion of any of the parameters eventually a meaningless
497 comparison amongst documented photocatalysts. In order to establish a real-time applicability, it
498 is strongly advised to evaluate the activity a photocatalyst with the documented literature. To take
499 these aspects into consideration, we generated a comparison factor (CF) to serve as an example of
500 a comparative study.[47,51] The CF values are based on the ability to transform a large amount of
501 pollutants (in the numerator) while using a minimal amount of energy and raw materials (in the
502 denominator), as evaluated by the **Eq. 5**. Accordingly, CF factors of various photocatalysts were
503 compared with the reported literatures. The CF value of dDAAQ-TFP is 10.28, which is 26582,
504 243, 10 and 10 times greater than the COF-HTBB,[7] MWCNT,[3] Tp-Mela,[2] and CN_{600},[5] respectively.
505 Most recently, Tp-Mela COF has been shown to be a highly effective metal-free carbonaceous
506 photocatalyst for Fenton-like photodegradation. The results are superior to those of numerous
507 metal-based catalysts, such as FeOOH, Fe_3O_4, α-Fe_2O_3, and FeS_2. We are really delighted to know
508 that, the activity of dDAAQ-TFP even outperformed the results as shown in the **Figure 8d**.

$$Comparision\ factor\ (CF) = \frac{[Pollutant] \times Removal\ efficiecncy}{[catalyst] \times [H_2O_2] \times Source\ power \times Time} \qquad \text{Eq. 5}$$

509 **Evaluation of reaction mechanism:**

510 To obtain further insight into the degradation mechanism, we have performed a series of
511 scavenging tests. For instance, gaseous oxygen (O_2), deprotonated disodium
512 ethylenediaminetetraacetate dihydrate (EDTA-Na_2), p-benzoquinone (p-BQ), sodium azide (NaN_3)
513 and tert-butyl alcohol (TBA) were employed as scavenging agents for trapping excited electrons
514 (e^-), holes (h^+), superoxide radical anion ($O_2^{\bullet-}$), singlet oxygen ($^1O_2$) and hydroxyl radicals ($^{\bullet}OH$)
515 respectively.

516 Under the visible light, the semiconducting dDAAQ-TFP (E_g = 2.07 eV) is excited forming highly
517 reactive electrons (e^-) and holes (h^+) in conduction (CB) and valance band (VB) respectively (**Eq.**
518 **6**).

$$dDAAQ - TFP + hv \rightarrow CB\ (e^-) + VB\ (h^+) \qquad \text{Eq. 6}$$
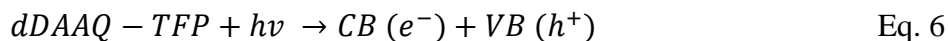
519   H_2O_2 is a stronger one electron oxidant with the potential of E_0 (H_2O_2/·OH) = +0.71 V vs NHE].[52,53]

520   The dDAAQ-TFP possesses suitable CB potentials of -0.92 V vs NHE that is sufficient for

521   activation of H_2O_2 via direct single electron reduction process (**Eq. 7**).

$$CB\ (e^-) +\ H_2O_2\ \rightarrow\ OH^- +\ ^\cdot OH \qquad\qquad \text{Eq. 7}$$
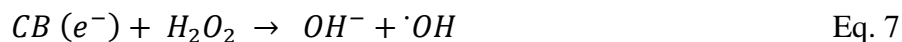
522   Molecular oxygen is a moderate electron scavenging agent [E_0 (O_2/O_2·⁻) = -0.33 V vs NHE]. Thus,

523   the contribution of excited electrons was confirmed via pursing molecular oxygen gas through the

524   reaction mixture. The rate constant of MB degradation was significantly reduced to $k = 1.08 \times 10^{-1}$

525   ^{1} min^{-1} via the oxygen reduction reaction (ORR). ORR produces weaker oxidant O_2·⁻ (see **Eq. 8**)

526   than ·OH radicals (E_0 = +2.8 V vs NHE).[54] Alternatively, molecular oxygen suppresses the

527   generation of ·OH radicals via inhibiting the **Eq. 7** and thereby reduced MB degradation was

528   observed. The role of the O_2·⁻ radicals was also evident. Therefore, the reaction rate was

529   decelerated in presence of p-BQ as shown in the **Figure 9a** and **Eq. 8**.

$$O_2 +\ e^- \rightarrow\ O_2^{\bullet -} \qquad\qquad \text{Eq. 8}$$

530   Furthermore, the rate constant was reduced to $k = 1.42 \times 10^{-1}$ min^{-1} and $k = 8.05 \times 10^{-2}$ min^{-1} upon

531   addition of TBA and EDTA-2Na respectively indicating ·OH and hole mediated degradation as

532   represented in the **Eq. 9** and **Eq. 11**. Also, the latter case implies that H_2O_2 is directly activated by

533   holes forming moderately oxidizing O_2·⁻ anionic radical according to equation expressed (**Eq. 10**).[2]
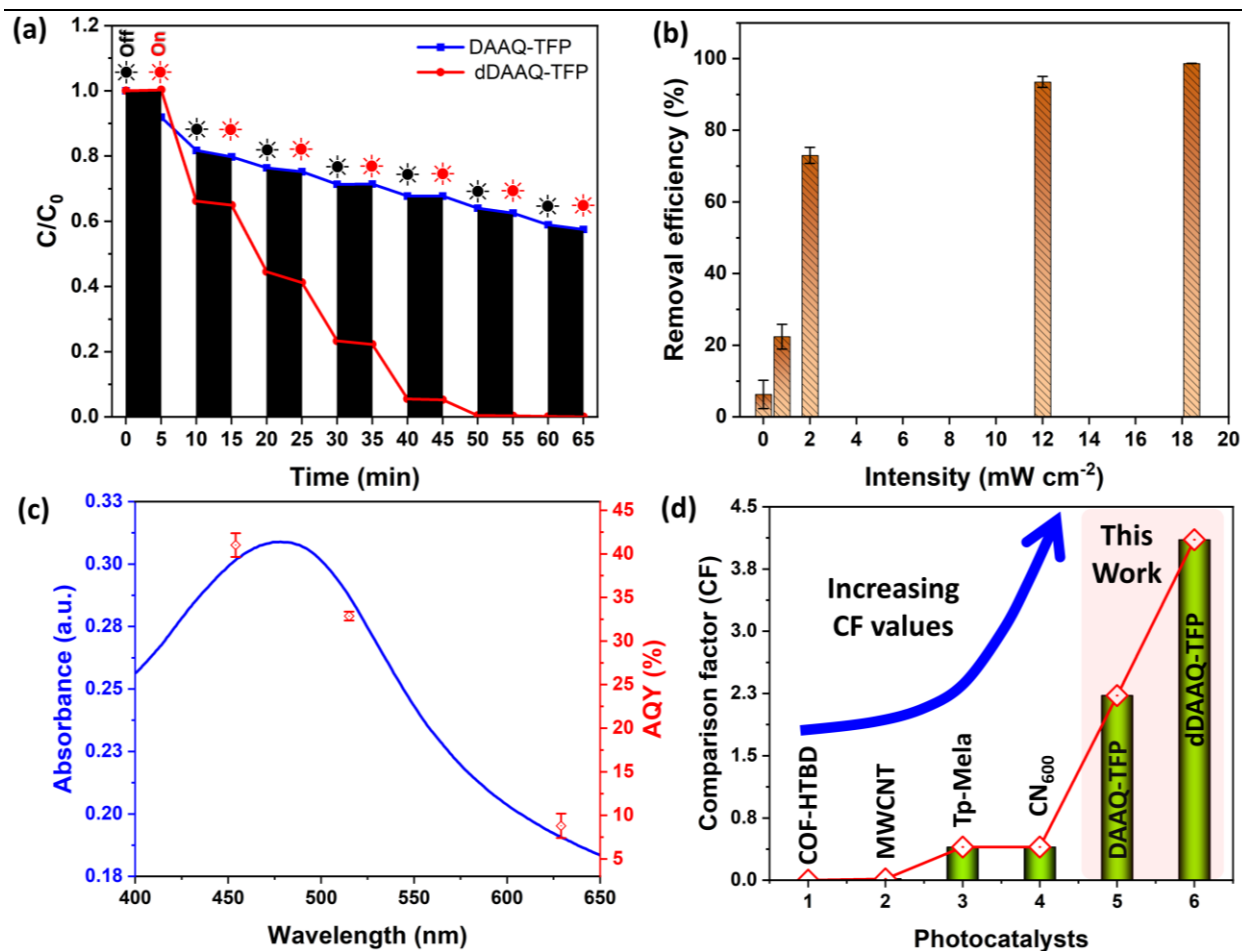
Figure 8: Influence of visible light in Fenton-like reactions for MB degradation: (a) transient on-off activities, (b) impact of visible light intensities, (c) action spectrum at various wavelengths, and (d) comparison of CF values. Reaction conditions: $[MB]^* = 98.2$ ppm, $[H_2O_2] = 0.15$ M, photocatalyst = 0.1 g L^{-1}, LED and T = RT.

*With the exception of MB for MWCNT, RhB was utilized to analyze CF values for all photocatalysts.

534

535 To investigate the role of holes, we performed the Fenton-like degradation both at lower (pH = 3)
536 and higher pH (pH = 10) than the ideal condition. The evaluated rate constants per minutes are
537 represented in increasing order as 8.49×10^{-2} (pH = 3) < 2.05×10^{-1} (pH = 7) < 3.07×10^{-1} (pH =
538 10). It is evident from the **Figure 9b** and **Figure S18** that the degradation of MB is significantly
539 improved at higher pH. Thus, it can be explained as the oxidation of OH^- by photoinduced holes
540 generates ˙OH radical enhances the photocatalytic degradation reaction (**Eq. 11**).[55] This is quiet
541 clear enough to correlate the formation of ˙OH via hole mediated oxidation of OH^- derived from
542 the **Eq. 7**. The oxidation of OH^- anion is represented by the **Eq. 9**. On contrary, direct oxidation of
543 H_2O is not possible as the dDAAQ-TFP possessed mismatched band of +1.1 (V vs NHE) that is
544 impossible to generate ˙OH radicals [E_0 (H_2O/˙OH) = +2.80V vs NHE].[52]
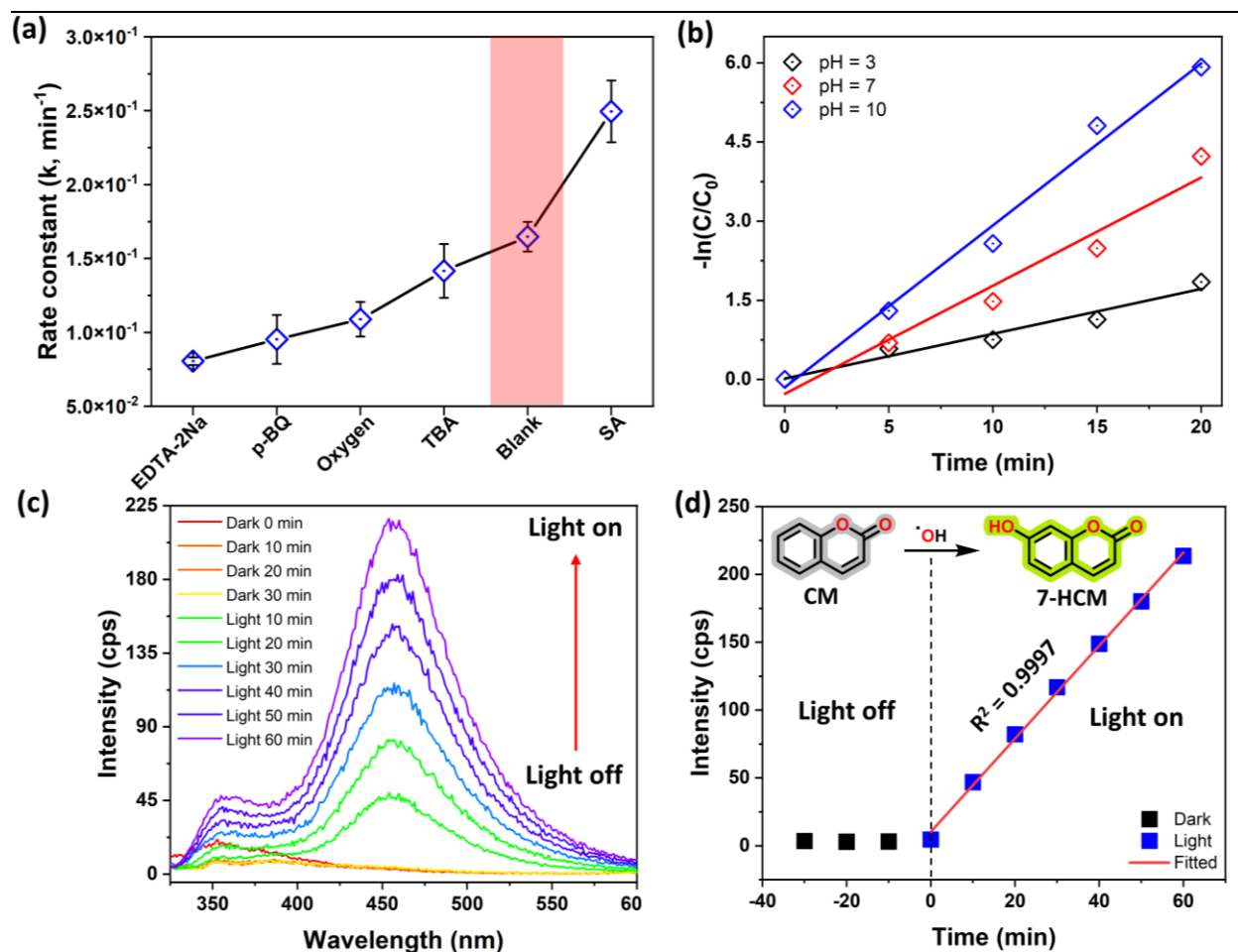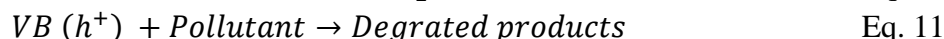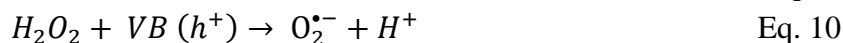
545

Figure 9: Evaluation of mechanism for photocatalytic Fenton-like reaction using dDAAQ-TFP: (a) contribution of various ROS with scavenging test: [EDTA-2Na] = 5 mM, [p-BQ] = 20 mM, [Oxygen] > 1 atm, [TBA] = 20 mM and [SA] = 20 mM; (b) pH dependent study for MB degradation. Reaction conditions: [MB] = 115 ppm, [catalyst] = 0.1 g L^{-1}, [H$_2$O$_2$] = 0.15 M, T = RT, Detection of hydroxyl radical using coumarin probe: (c) and (d) activity under light off and on conditions linearly fitted plot. Reaction conditions: [coumarin] 5×10^{-4} M, [Catalyst] = 0.1 g L^{-1}.

546

$$OH^- + VB\ (h^+) \rightarrow\ ^{\cdot}OH \qquad\qquad \text{Eq. 9}$$
$$H_2O_2 + VB\ (h^+) \rightarrow\ O_2^{\bullet-} + H^+ \qquad\qquad \text{Eq. 10}$$
$$VB\ (h^+) + Pollutant \rightarrow Degrated\ products \qquad\qquad \text{Eq. 11}$$

547   It is noteworthy to mention that the photo-Fenton reactions show the higher degradation capability
548   usually at acidic pH unlike the known literatures.[2,4] dDAAQ-TFP shows highly effective activity
549   of the photocatalyst even with high pH tolerance. In addition, it is evident from the **Figure 9a** that
550   the $^1O_2$ does not contribute to the rate limiting step which was confirmed upon trapping experiment
551   with SA. The degradation rate was remarkably enhanced as compared to the controlled reaction (k
552     $= 2.5 \times 10^{-1}$ min^{-1}). The acceleration of MB degradation could be generation of azide radicals ($^{\cdot}N_3$).
553   SA produces $^{\cdot}N_3$ radicals, which could be is a secondary reactive species for MB degradation as
554   reported.[56]
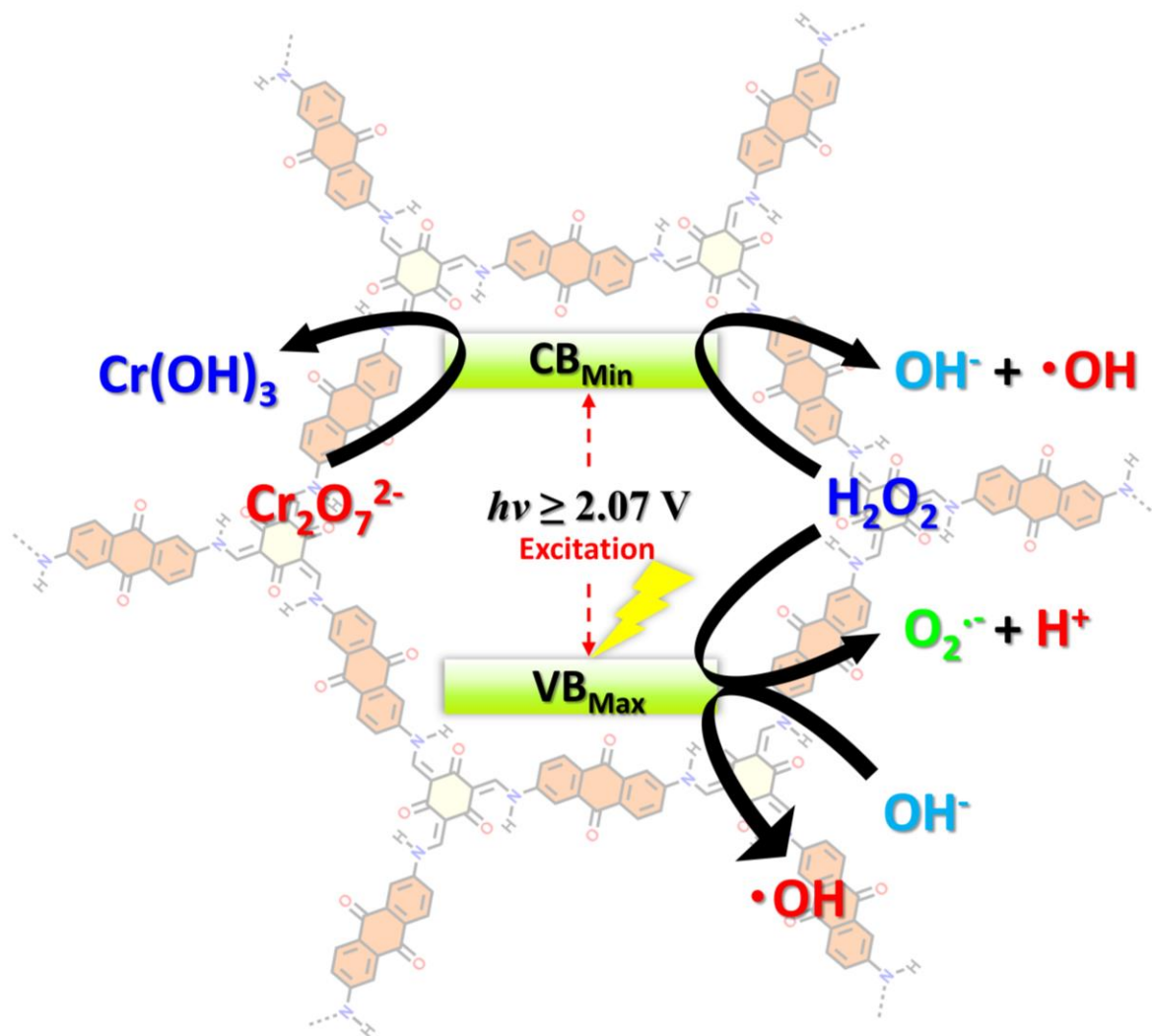
Scheme 2: Plaussible mechanism for photocatalytic reduction and Fenton-like reactions.

555

556   The evidence for generation of ·OH and $O_2^{·-}$ generation was further clarified via a probe-radical
557   integration experiment using fluorescence spectroscopy.[57] Coumarin (CM) was used as a selective
558   probe to examine their generation in photocatalytic system. In fact, these radicals react with less
559   fluorescent coumarin molecules and produces highly fluorescent 7-hydroxycoumarin adduct (7-
560   HCM) that emits at ~λ_{max} = 457 nm. Initially, 7-HCM adduct produced was insignificant under
561   dark conditions as shown in the **Figure 9c** and **Figure 9d**. When the light was turned on, the
562   fluorescence intensity was linearly (linear fit, R^2 = 0.99782) increased. The higher the
563   concentration of the radicals produced implies higher concentrations of the coumarin oxidation.
564   Thus, the results clearly confirm the contribution ·OH and $O_2^{·-}$ towards MB degradation via
565   photocatalytic activation of H_2O_2. In summary, dDAAQ-TFP generates electron and holes when
566   excited with the energy ≥2.07 eV, i.e., the band bap of dDAAQ-TFP. The excited electron and
567   holes respectively produce ·OH and $O_2^{·-}$ radical species via activation of H_2O_2. Eventually, the
568   degradation of organic pollutants is caused by the generation of highly reactive oxygen species.

569 Given the information from the aforementioned studies, the schematically depicted mechanism for
570 both the reduction of Cr^{6+} (left) and Fenton-like reactions (right) as shown in the **Scheme 2**.

571 Visible light irradiation often undergoes photobleaching of colored organic pollutants instead of
572 complete degradation.[58,59] For instance, when exposed to visible light, MB is converted to the
573 colorless leuco-MB (LMB) form by transferring an excited electron. In contrast, the color could
574 be regenerated under the exposure of air. This is possible via back electron transfer from LMB to
575 the photocatalyst reversibly under the influence of oxygen. To examine the reversibility in the
576 photo Fenton-like reaction, we employed the degradation and regeneration experiments initially
577 in absence air and then switched to pursing O_2 atmospheres subsequently. As anticipated, after 25
578 minutes of irradiation, a sequential MB deterioration was observed (>99%) with absence of air.
579 Conversely, despite constant oxygen infusion into the degraded solution, we did not observe
580 color reappeared. This was further confirmed by using absorbance spectroscopy as displayed in
581 the **Figure S19**. Therefore, dDAAQ-TFP induces photocatalysis rather than photobleaching under
582 visible light.

583 **Recyclability and reusability test:**

584 One of the most crucial characteristics of catalytic materials is their ability to be recycled and
585 reused. Therefore, it is strongly advised that catalytic materials can be recovered and afterwards
586 reused after additional cycles in order to reduce preparation time and expenses. Several well-
587 known catalytic processes utilized in the chemical industry today use metals, notably precious
588 metals, or metal oxides as catalysts. Unfortunately, the possibility of leaching limits the use of
589 metal-based catalytic systems for practical applications. In this instance, there are several reports
590 that refer to potential health hazards even in the presence of residual metal content.[51] Additionally,
591 these are quite expensive and often require post-application purification using cutting-edge
592 technologies. In contrast, metal-free systems often outperform conventional ones without the
593 assistance of metal constituents and thereby the obvious lower risks for health and environmental
594 issues. As previously described by Banerjee et al., the β-ketoenamine-linkage in COF materials is
595 highly chemically stable via the combination of reversible/irreversible pathways,.[60] The findings
596 shown that such connection in imine-based COF is sustainable up to 9N in both acidic and alkaline
597 environments. As a result, our curiosity was extended to examine the photocatalytic activities after
598 successive cycles. We speculated that the ground form of dDAAQ-TFP could work well as a
599 photocatalyst, particularly for Fenton-like reactions. Therefore, the ground photocatalyst was
600 employed for Cr^{6+} reduction and Fenton-like degradation of MB under visible light. The
601 photocatalytic applications were conducted similarly as discussed earlier in the ESI. As expected,
602 the removal efficiency of Cr^{6+} and MB were more than 96 and 99% respectively even after 5th
603 cycles of usages. In contrast to the photo Fenton-like reaction, a negligible weight loss was found
604 for the photoreduction of Cr^{6+}. Nevertheless, as can be seen from **Figure S20**, the results are as
605 similar as the initial cycles. Eventually, the ground COF is proven to be a reusable and effective
606 photocatalyst for both applications. Once the reaction was finished, the photocatalyst was
607 recovered by centrifugation, washed properly from the reaction, and dried for the subsequent run.

608   Additionally, the crystallinity and chemical properties of recovered materials were examined after
609   5th cycles of application. From the powder XRD pattern, the chemical crystallinity of the imine-
610   based COF is retained especially after the photocatalytic reduction of Cr^{3+} while a relatively
611   negligible changes was observed for photo Fenton-like degradation shown in the **Figure S21**.
612   Furthermore, FT-IR analysis shows the primary peaks corresponding to the C-N and C=O of
613   dDAAQ-TFP is preserved after Fenton-like degradation. A broad stretching band at 1060 cm^{-1} was
614   also observed which probably indicates the remnant molecular fragments of sulfoxide (S=O) after
615   MB degrdation.[61] Besides, a strong O-H stretching peak is also observed in the range (3725-3000
616   cm^{-1}) which correspond to the remnant trapped moistures. In contrast, Cr-residual was found in
617   the XPS spectrum following the first run of the photoreduction reaction (**Figure S22**). The narrow
618   scan XPS spectrum reveals the residual as Cr^{3+} oxidation state (inset **Figure S22**). Furthermore,
619   ICP-MS analysis of the material was performed to quantify the Cr-residuals present after first
620   cycles. Only **0.0181** ppm of the Cr-residuals were obtained in dDAAQ-TFP. It is worth noting that
621   the effect of its presence had no apparent effect on the reduction rate even after 5th cycle of usage
622   (see **Figure S20**).

Photo-Fenton like activities in continuous flow approach:

624   With the advent of flow chemistry, new opportunities have arisen regarding the commercialization
625   of batch-processed products. Owing to the advantageous features of high efficiency, easy
626   scalability, simple operation and low-cost technology, continuous flow reactions has proven to be
627   an alternative strategy to excel many applications including photocatalysis. Over the past decades,
628   photocatalytic systems are implemented in continuous flow to elevate effectivity of conventional
629   batch reactions.[62–66] Accordingly, we have extended the photo-Fenton-like experiments in a glass
630   capillary based continuous flow micreactor (**Figure 10a** and **Figure S24**). To evaluate the effect
631   of flow rate on the photocatalytic activities, the polluted water was flown at various volumetric
632   flow rates (10, 100, 300 and 500 μL min^{-1}) using a programmable syringe pump. It could be
633   observed that the MB (98.2 ppm) is completely removed at lower flow rates i.e., 10 and 100 μL
634   min[-1]. In contrast, a subsequent decrement in the photocatalytic efficiency was appeared at higher
635   flow rates i.e., 94% and 46% for 300 and 500 μL min^{-1} respectively (**Figure 10b**). It is probably
636   due to the longer residence time of pollutants experiences higher contact time with visible light
637   irradiation at slower flow rate of infusion. The calculated residence times corresponding to the
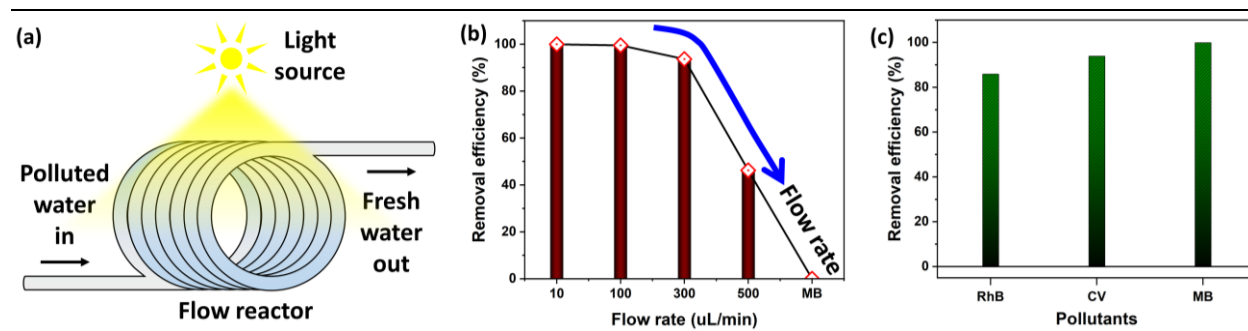638   various flow rate was represented in **Table S5**.[67]

Figure 10: Photo Fenton-like reaction performed in continuous flow: (a) schematic representation of continuous flow system, and continuous degradation organic pollutants in glass flow reactor: (b) effect of flow rate in MB, and (c) removal efficiency for various pollutants. Reaction conditions: [Pollutant] = 98.19 ppm, [H_2O_2] = 0.15 M, photocatalyst = 0.1 g L^{-1}, white LED and T = RT.

It is imperative to note that the PSTY was determined to be 93.35 at 100 L min^{-1}, which is 28 times more effective than the traditional batch technique (PSTY = 3.33). The versatility of the continuous flow photo Fenton-like degradation was also implemented to other organic pollutants as shown in **Figure 10c**. Under the identical conditions, the photocatalytic activities for RhB and CV were 86% and 95% at 100 μL min^{-1}. Thus, the results show a promising photocatalytic candidature of the dDAAQ-TFP for large scale applicability.

Conclusions

We have demonstrated that the mechanically pulverized covalent organic framework amplified photocatalytic activities in visible light. Pulverization induces aggregation of fibrous COF that increases excited electron density for easier charge carrier mobility. In visible light, the pulverized COF shown improved stability for electrons and holes, which efficiently produces highly reactive species (e^-, h^+, $O_2^{\bullet-}$ and $^\bullet OH$) via effective activation of H_2O_2. Even at relatively low concentrations of H_2O_2, the photocatalyst outperformed for a noticeably high level of pollutant degradation. A startlingly high apparent quantum yield (~41%) was still attained even with a decreased concentration of the photocatalyst. The metal-free photocatalyst alone exhibited an extremely high activity unlike the metal-based photocatalysts that requires acidic pH. The reactivity of pulverized COF is improved for photoreduction of hexavalent chromium as well. The β-ketoenamine linked COF demonstrated chemical stability and long-term usability as a heterogeneous photocatalyst for photocatalytic reduction and Fenton-like reactions. The photocatalyst additionally outperformed the Fenton-like degradation in a continuous flow system, demonstrating its potential application for industrial scalability and sustainable economic growth.

Conflicts of interest

The authors declare no conflict of interest.

Declaration of Competing Interest

The authors affirm that they have no known financial or interpersonal conflicts that might have appeared to have influenced the research presented in this study.

Acknowledgements

ORCID

Rituporn Gogoi: 0000-0003-4652-4013

Swadhin Kumar Jena: 0000-0002-1197-5036

Astha Singh: 0000-0001-7080-1477

Kajal Sharma: 0000-0002-5767-1767

Prem Felix Siril: 0000-0002-8818-7310

References

(1)   Zhu, Y.; Fan, W. H.; Feng, W. Y.; Wang, Y.; Liu, S.; Dong, Z. M.; Li, X. M. A Critical Review on Metal Complexes Removal from Water Using Methods Based on Fenton-like Reactions: Analysis and Comparison of Methods and Mechanisms. *J Hazard Mater* **2021**, *414*, 125517. https://doi.org/10.1016/J.JHAZMAT.2021.125517.

(2)   Liao, Q.; Wang, D.; Ke, C.; Zhang, Y.; Han, Q.; Zhang, Y.; Xi, K. Metal-Free Fenton-like Photocatalysts Based on Covalent Organic Frameworks. *Appl Catal B* **2021**, *298*, 120548. https://doi.org/10.1016/J.APCATB.2021.120548.

(3)   Tolba, A.; Gar Alalm, M.; Elsamadony, M.; Mostafa, A.; Afify, H.; Dionysiou, D. D. Modeling and Optimization of Heterogeneous Fenton-like and Photo-Fenton Processes Using Reusable Fe3O4-MWCNTs. *Process Safety and Environmental Protection* **2019**, *128*, 273–283. https://doi.org/10.1016/J.PSEP.2019.06.011.

(4)   Espinosa, J. C.; Navalón, S.; Álvaro, M.; García, H. Reduced Graphene Oxide as a Metal-Free Catalyst for the Light-Assisted Fenton-Like Reaction. *ChemCatChem* **2016**, *8* (16), 2642–2648. https://doi.org/10.1002/CCTC.201600364.

(5)   Cui, Y.; Ding, Z.; Liu, P.; Antonietti, M.; Fu, X.; Wang, X. Metal-Free Activation of H2O2 by g-C3N4 under Visible Light Irradiation for the Degradation of Organic Pollutants. *Physical Chemistry Chemical Physics* **2012**, *14* (4), 1455–1462. https://doi.org/10.1039/C1CP22820J.

(6)   Yue, D.; Qian, X.; Kan, M.; Fang, M.; Jia, J.; Yang, X.; Zhao, Y. A Metal-Free Visible Light Active Photo-Electro-Fenton-like Cell for Organic Pollutants Degradation. *Appl Catal B* **2018**, *229*, 211–217. https://doi.org/10.1016/J.APCATB.2018.02.033.

705 (7)   Liu, C.; Chen, M.; Li, H.; Shi, Q.; Feng, Y.; Zhang, B. Crystalline Covalent Organic
706   Frameworks Based on Mixed Metallo- and Tetrahydroporphyrin Monomers for Use as
707   Efficient Photocatalysts in Dye Pollutant Removal. *Cryst Growth Des* **2022**, *22* (8), 4745–
708   4756.
709   https://doi.org/10.1021/ACS.CGD.2C00046/ASSET/IMAGES/LARGE/CG2C00046_000
710   7.JPEG.

711 (8)   Li, C.; Liu, J.; Li, H.; Wu, K.; Wang, J.; Yang, Q. Covalent Organic Frameworks with
712   High Quantum Efficiency in Sacrificial Photocatalytic Hydrogen Evolution. *Nature
713   Communications 2022 13:1* **2022**, *13* (1), 1–9. https://doi.org/10.1038/s41467-022-30035-
714   x.

715 (9)   Vyas, V. S.; Haase, F.; Stegbauer, L.; Savasci, G.; Podjaski, F.; Ochsenfeld, C.; Lotsch, B.
716   v. A Tunable Azine Covalent Organic Framework Platform for Visible Light-Induced
717   Hydrogen Generation. *Nature Communications 2015 6:1* **2015**, *6* (1), 1–9.
718   https://doi.org/10.1038/ncomms9508.

719 (10) Li, L.; Fang, W.; Zhang, P.; Bi, J.; He, Y.; Wang, J.; Su, W. Sulfur-Doped Covalent
720   Triazine-Based Frameworks for Enhanced Photocatalytic Hydrogen Evolution from Water
721   under Visible Light. *J Mater Chem A Mater* **2016**, *4* (32), 12402–12406.
722   https://doi.org/10.1039/C6TA04711D.

723 (11) Chen, J.; Tao, X.; Tao, L.; Li, H.; Li, C.; Wang, X.; Li, C.; Li, R.; Yang, Q. Novel
724   Conjugated Organic Polymers as Candidates for Visible-Light-Driven Photocatalytic
725   Hydrogen Production. *Appl Catal B* **2019**, *241*, 461–470.
726   https://doi.org/10.1016/J.APCATB.2018.09.011.

727 (12) Ding, S. Y.; Wang, P. L.; Yin, G. L.; Zhang, X.; Lu, G. Energy Transfer in Covalent
728   Organic Frameworks for Visible-Light-Induced Hydrogen Evolution. *Int J Hydrogen
729   Energy* **2019**, *44* (23), 11872–11876. https://doi.org/10.1016/J.IJHYDENE.2019.03.039.

730 (13) Gan, S. X.; Jia, C.; Qi, Q. Y.; Zhao, X. A Facile and Scalable Synthetic Method for
731   Covalent Organic Nanosheets: Ultrasonic Polycondensation and Photocatalytic
732   Degradation of Organic Pollutants. *Chem Sci* **2022**, *13* (4), 1009–1015.
733   https://doi.org/10.1039/D1SC05504F.

734 (14) Wang, D.; Li, X.; Zheng, L. L.; Qin, L. M.; Li, S.; Ye, P.; Li, Y.; Zou, J. P. Size-
735   Controlled Synthesis of CdS Nanoparticles Confined on Covalent Triazine-Based
736   Frameworks for Durable Photocatalytic Hydrogen Evolution under Visible Light.
737   *Nanoscale* **2018**, *10* (41), 19509–19516. https://doi.org/10.1039/C8NR06691D.

738 (15) Lv, Y.; Liu, Y.; Ye, X.; Liu, G.; Tao, X. The Effect of Mechano-Stimuli on the
739   Amorphous-to-Crystalline Transition of Mechanochromic Luminescent Materials.
740   *CrystEngComm* **2014**, *17* (3), 526–531. https://doi.org/10.1039/C4CE01212G.

741 (16) Guo, S.; Zhang, G.; Kong, L.; Tian, Y.; Yang, J. Molecular Packing-Controlled
742   Mechanical-Induced Emission Enhancement of Tetraphenylethene-Functionalised

743 Pyrazoline Derivatives. *Chemistry – A European Journal* **2020**, *26* (17), 3834–3842.
744 https://doi.org/10.1002/CHEM.201905256.

745 (17) Dong, Y.; Xu, B.; Zhang, J.; Tan, X.; Wang, L.; Chen, J.; Lv, H.; Wen, S.; Li, B.; Ye, L.;
746 Zou, B.; Tian, W. Piezochromic Luminescence Based on the Molecular Aggregation of
747 9,10-Bis((E)-2-(Pyrid-2-Yl)Vinyl)Anthracene. *Angewandte Chemie - International*
748 *Edition* **2012**, *51* (43), 10782–10785. https://doi.org/10.1002/ANIE.201204660.

749 (18) Deblase, C. R.; Silberstein, K. E.; Truong, T. T.; Abruña, H. D.; Dichtel, W. R. β-
750 Ketoenamine-Linked Covalent Organic Frameworks Capable of Pseudocapacitive Energy
751 Storage. *J Am Chem Soc* **2013**, *135* (45), 16821–16824.
752 https://doi.org/10.1021/ja409421d.

753 (19) Li, Q.; Lan, X.; An, G.; Ricardez-Sandoval, L.; Wang, Z.; Bai, G. Visible-Light-
754 Responsive Anthraquinone Functionalized Covalent Organic Frameworks for Metal-Free
755 Selective Oxidation of Sulfides: Effects of Morphology and Structure. *ACS Catal* **2020**, *10*
756 (12), 6664–6675.
757 https://doi.org/10.1021/ACSCATAL.0C00290/ASSET/IMAGES/LARGE/CS0C00290_0
758 009.JPEG.

759 (20) Li, Y.; Ding, Z.; Zhang, X.; Li, J.; Liu, X.; Lu, T.; Yao, Y.; Pan, L. Novel Hybrid
760 Capacitive Deionization Constructed by a Redox-Active Covalent Organic Framework
761 and Its Derived Porous Carbon for Highly Efficient Desalination. *J Mater Chem A Mater*
762 **2019**, *7* (44), 25305–25313. https://doi.org/10.1039/C9TA07344B.

763 (21) Li, Q.; Lan, X.; An, G.; Ricardez-Sandoval, L.; Wang, Z.; Bai, G. Visible-Light-
764 Responsive Anthraquinone Functionalized Covalent Organic Frameworks for Metal-Free
765 Selective Oxidation of Sulfides: Effects of Morphology and Structure. *ACS Catal* **2020**, *10*
766 (12), 6664–6675. https://doi.org/10.1021/acscatal.0c00290.

767 (22) Chandra, S.; Kandambeth, S.; Biswal, B. P.; Lukose, B.; Kunjir, S. M.; Chaudhary, M.;
768 Babarao, R.; Heine, T.; Banerjee, R. Chemically Stable Multilayered Covalent Organic
769 Nanosheets from Covalent Organic Frameworks via Mechanical Delamination. *J Am*
770 *Chem Soc* **2013**, *135* (47), 17853–17861.
771 https://doi.org/10.1021/JA408121P/SUPPL_FILE/JA408121P_SI_001.PDF.

772 (23) Karak, S.; Kandambeth, S.; Biswal, B. P.; Sasmal, H. S.; Kumar, S.; Pachfule, P.;
773 Banerjee, R. Constructing Ultraporous Covalent Organic Frameworks in Seconds via an
774 Organic Terracotta Process. *J Am Chem Soc* **2017**, *139* (5), 1856–1862.
775 https://doi.org/10.1021/JACS.6B08815/SUPPL_FILE/JA6B08815_SI_002.CIF.

776 (24) Bu, Y.; Chen, Z.; Xie, T.; Li, W.; Ao, J. P. Fabrication of C3N4 Ultrathin Flakes by
777 Mechanical Grind Method with Enhanced Photocatalysis and Photoelectrochemical
778 Performance. *RSC Adv* **2016**, *6* (53), 47813–47819. https://doi.org/10.1039/C6RA05524A.

779 (25) Hauschild, D.; Handick, E.; Göhl-Gusenleitner, S.; Meyer, F.; Schwab, H.; Benkert, A.;
780 Pohlner, S.; Palm, J.; Tougaard, S.; Heske, C.; Weinhardt, L.; Reinert, F. Band-Gap

781   Widening at the Cu(In,Ga)(S,Se)2 Surface: A Novel Determination Approach Using
782   Reflection Electron Energy Loss Spectroscopy. *ACS Appl Mater Interfaces* **2016**, *8* (32),
783   21101–21105. https://doi.org/10.1021/acsami.6b06358.

784 (26)   Liu, G.; Jaegermann, W.; He, J.; Sundström, V.; Sun, L. XPS and UPS Characterization of
785   the TiO2/ZnPcGly Heterointerface: Alignment of Energy Levels. *Journal of Physical*
786   *Chemistry B* **2002**, *106* (23), 5814–5819.
787   https://doi.org/10.1021/JP014192B/ASSET/IMAGES/LARGE/JP014192BF00006.JPEG.

788 (27)   Wang, Z.; Yang, X.; Yang, T.; Zhao, Y.; Wang, F.; Chen, Y.; Zeng, J. H.; Yan, C.;
789   Huang, F.; Jiang, J. X. Dibenzothiophene Dioxide Based Conjugated Microporous
790   Polymers for Visible-Light-Driven Hydrogen Production. *ACS Catal* **2018**, *8* (9), 8590–
791   8596. https://doi.org/10.1021/ACSCATAL.8B02607/ASSET/IMAGES/LARGE/CS-
792   2018-02607X_0005.JPEG.

793 (28)   Dolenko, T. A.; Burikov, S. A.; Vervald, A. M.; Vlasov, I. I.; Dolenko, S. A.; Laptinskiy,
794   K. A.; Rosenholm, J. M.; Shenderova, O. A. Optical Imaging of Fluorescent Carbon
795   Biomarkers Using Artificial Neural Networks.
796   *https://doi.org/10.1117/1.JBO.19.11.117007* **2014**, *19* (11), 117007.
797   https://doi.org/10.1117/1.JBO.19.11.117007.

798 (29)   Xu, D.; Wang, Y.; Li, L.; Zhou, H.; Liu, X. Aggregation-Induced Enhanced Emission-
799   Type Cruciform Luminophore Constructed by Carbazole Exhibiting Mechanical Force-
800   Induced Luminescent Enhancement and Chromism. *RSC Adv* **2020**, *10* (20), 12025–
801   12034. https://doi.org/10.1039/D0RA00283F.

802 (30)   Zhitkovich, A. Chromium in Drinking Water: Sources, Metabolism, and Cancer Risks.
803   *Chem Res Toxicol* **2011**, *24* (10), 1617–1629.
804   https://doi.org/10.1021/TX200251T/ASSET/IMAGES/LARGE/TX-2011-
805   00251T_0003.JPEG.

806 (31)   Li, Y.; Bian, Y.; Qin, H.; Zhang, Y.; Bian, Z. Photocatalytic Reduction Behavior of
807   Hexavalent Chromium on Hydroxyl Modified Titanium Dioxide. *Appl Catal B* **2017**, *206*,
808   293–299. https://doi.org/10.1016/J.APCATB.2017.01.044.

809 (32)   Chen, W.; Yang, Z.; Xie, Z.; Li, Y.; Yu, X.; Lu, F.; Chen, L. Benzothiadiazole
810   Functionalized D–A Type Covalent Organic Frameworks for Effective Photocatalytic
811   Reduction of Aqueous Chromium(VI). *J Mater Chem A Mater* **2019**, *7* (3), 998–1004.
812   https://doi.org/10.1039/C8TA10046B.

813 (33)   Miretzky, P.; Cirelli, A. F. Cr(VI) and Cr(III) Removal from Aqueous Solution by Raw
814   and Modified Lignocellulosic Materials: A Review. *J Hazard Mater* **2010**, *180* (1–3), 1–
815   19. https://doi.org/10.1016/J.JHAZMAT.2010.04.060.

816 (34)   Costa, M. Potential Hazards of Hexavalent Chromate in Our Drinking Water. *Toxicol*
817   *Appl Pharmacol* **2003**, *188* (1), 1–5. https://doi.org/10.1016/S0041-008X(03)00011-5.

818   (35)   Ghosh, R.; Gopalakrishnan, S.; Renganathan, T.; Pushpavanam, S. Adsorptive
819   Colorimetric Determination of Chromium(VI) Ions at Ultratrace Levels Using Amine
820   Functionalized Mesoporous Silica. *Scientific Reports 2022 12:1* **2022**, *12* (1), 1–11.
821   https://doi.org/10.1038/s41598-022-09689-6.

822   (36)   Borthakur, P.; Das, M. R.; Szunerits, S.; Boukherroub, R. CuS Decorated Functionalized
823   Reduced Graphene Oxide: A Dual Responsive Nanozyme for Selective Detection and
824   Photoreduction of Cr(VI) in an Aqueous Medium. *ACS Sustain Chem Eng* **2019**, *7* (19),
825   16131–16143.
826   https://doi.org/10.1021/ACSSUSCHEMENG.9B03043/ASSET/IMAGES/LARGE/SC9B0
827   3043_0009.JPEG.

828   (37)   Shiraishi, Y.; Ueda, Y.; Soramoto, A.; Hinokuma, S.; Hirai, T. Photocatalytic Hydrogen
829   Peroxide Splitting on Metal-Free Powders Assisted by Phosphoric Acid as a Stabilizer.
830   *Nature Communications 2020 11:1* **2020**, *11* (1), 1–9. https://doi.org/10.1038/s41467-020-
831   17216-2.

832   (38)   Ghasimi, S.; Prescher, S.; Wang, Z. J.; Landfester, K.; Yuan, J.; Zhang, K. A. I.
833   Heterophase Photocatalysts from Water-Soluble Conjugated Polyelectrolytes: An
834   Example of Self-Initiation under Visible Light. *Angewandte Chemie - International*
835   *Edition* **2015**, *54* (48), 14549–14553. https://doi.org/10.1002/ANIE.201505325.

836   (39)   Huang, W.; Liu, N.; Zhang, X.; Wu, M.; Tang, L. Metal Organic Framework G-
837   C3N4/MIL-53(Fe) Heterojunctions with Enhanced Photocatalytic Activity for Cr(VI)
838   Reduction under Visible Light. *Appl Surf Sci* **2017**, *425*, 107–116.
839   https://doi.org/10.1016/J.APSUSC.2017.07.050.

840   (40)   Zhuang, Q.; Chen, H.; Zhang, C.; Cheng, S.; Dong, W.; Xie, A. Rapid Chromium
841   Reduction by Metal-Free Organic Polymer Photocatalysis via Molecular Engineering. *J*
842   *Hazard Mater* **2022**, *434*, 128938. https://doi.org/10.1016/J.JHAZMAT.2022.128938.

843   (41)   Yan, X.; Ning, G.; Zhao, P. Enhanced Visible Light Photocatalytic Reduction of Cr(VI)
844   over a Novel Square Nanotube Poly(Triazine Imide)/TiO2 Heterojunction. *Catalysts*
845   *2019, Vol. 9, Page 55* **2019**, *9* (1), 55. https://doi.org/10.3390/CATAL9010055.

846   (42)   Gong, J.; Li, Y.; Zhao, Y.; Wu, X.; Wang, J.; Zhang, G. Metal-Free Polymeric (SCN)n
847   Photocatalyst with Adjustable Bandgap for Efficient Organic Pollutants Degradation and
848   Cr(VI) Reduction under Visible-Light Irradiation. *Chemical Engineering Journal* **2020**,
849   *402*, 126147. https://doi.org/10.1016/J.CEJ.2020.126147.

850   (43)   Wang, Y.; Liu, Y.; Bao, S.; Yu, Y.; Li, J.; Yang, W.; Xu, S.; Li, H. Aminated Metal-Free
851   Red Phosphorus Nanosheets for Adsorption and Photocatalytic Reduction of Cr(VI) from
852   Water. *Sep Purif Technol* **2021**, *274*, 118968.
853   https://doi.org/10.1016/J.SEPPUR.2021.118968.

854   (44)   Yi, X. H.; Wang, F. X.; Du, X. D.; Wang, P.; Wang, C. C. Facile Fabrication of BUC-
855   21/g-C3N4 Composites and Their Enhanced Photocatalytic Cr(VI) Reduction

856   Performances under Simulated Sunlight. *Appl Organomet Chem* **2019**, *33* (1), e4621.
857   https://doi.org/10.1002/AOC.4621.

858   (45)   Li, M.; Ramachandran, R.; Sakthivel, T.; Wang, F.; Xu, Z. X. Siloxene: An Advanced
859   Metal-Free Catalyst for Efficient Photocatalytic Reduction of Aqueous Cr(VI) under
860   Visible Light. *Chemical Engineering Journal* **2021**, *421*, 129728.
861   https://doi.org/10.1016/J.CEJ.2021.129728.

862   (46)   Chen, H.; Wang, X.; Li, J.; Wang, X. Cotton Derived Carbonaceous Aerogels for the
863   Efficient Removal of Organic Pollutants and Heavy Metal Ions. *J Mater Chem A Mater*
864   **2015**, *3* (11), 6073–6081. https://doi.org/10.1039/C5TA00299K.

865   (47)   Gogoi, R.; Mebansharai Dohling, H.; Singh, A.; Sharma, K.; Singh Sagara, P.; Felix Siril,
866   P. Visible Light Enhanced Photosynthesis of C-C Bonds Using PdO/Pd@PEDOT
867   Nanocomposite. *J Catal* **2022**, *414*, 109–124.
868   https://doi.org/10.1016/J.JCAT.2022.08.027.

869   (48)   Calza, P.; Minella, M.; Demarchis, L.; Sordello, F.; Minero, C. Photocatalytic Rate
870   Dependence on Light Absorption Properties of Different TiO2 Specimens. *Catal Today*
871   **2020**, *340*, 12–18. https://doi.org/10.1016/J.CATTOD.2018.10.013.

872   (49)   Xiao, Q.; Sarina, S.; Bo, A.; Jia, J.; Liu, H.; Arnold, D. P.; Huang, Y.; Wu, H.; Zhu, H.
873   Visible Light-Driven Cross-Coupling Reactions at Lower Temperatures Using a
874   Photocatalyst of Palladium and Gold Alloy Nanoparticles. *ACS Catal* **2014**, *4* (6), 1725–
875   1734. https://doi.org/10.1021/CS5000284/ASSET/IMAGES/LARGE/CS-2014-
876   000284_0007.JPEG.

877   (50)   Fatima, R.; Kim, J.-O. Photocatalytic Reduction of Chromium by Titanium Metal Organic
878   Frameworks in the Presence of Low-Molecular-Weight Organic Acids under UV and
879   Visible Light. *J Environ Chem Eng* **2022**, *10* (6), 108796.
880   https://doi.org/10.1016/j.jece.2022.108796.

881   (51)   Gogoi, R.; Singh, A.; Moutam, V.; Sharma, L.; Sharma, K.; Halder, A.; Siril, P. F.
882   Revealing the Unexplored Effect of Residual Iron Oxide on the Photoreforming Activities
883   of Polypyrrole Nanostructures on Plastic Waste and Photocatalytic Pollutant Degradation.
884   *J Environ Chem Eng* **2022**, *10* (2), 106649. https://doi.org/10.1016/J.JECE.2021.106649.

885   (52)   Sheng, J.; Li, X.; Xu, Y. Generation of H 2 O 2 and OH Radicals on Bi 2 WO 6 for
886   Phenol Degradation under Visible Light. **2014**. https://doi.org/10.1021/cs400927w.

887   (53)   Bi, D.; Xu, Y. Improved Photocatalytic Activity of WO 3 through Clustered Fe 2 O 3 for
888   Organic Degradation in the Presence of H 2 O 2. **2011**, *27*, 9359–9366.
889   https://doi.org/10.1021/la2012793.

890   (54)   Navalon, S.; de Miguel, M.; Martin, R.; Alvaro, M.; Garcia, H. Enhancement of the
891   Catalytic Activity of Supported Gold Nanoparticles for the Fenton Reaction by Light. *J*
892   *Am Chem Soc* **2011**, *133* (7), 2218–2226.
893   https://doi.org/10.1021/JA108816P/SUPPL_FILE/JA108816P_SI_001.PDF.

894   (55) Xue, W.; Bai, X.; Tian, J.; Ma, X.; Hu, X.; Fan, J.; Liu, E. Enhanced Photocatalytic H2
895   Evolution on Ultrathin Cd0.5Zn0.5S Nanosheets without a Hole Scavenger: Combined
896   Analysis of Surface Reaction Kinetics and Energy-Level Alignment. *Chemical*
897   *Engineering Journal* **2022**, *428*, 132608. https://doi.org/10.1016/J.CEJ.2021.132608.

898   (56) Katal, R.; Panah, S. M.; Saeedikhani, M.; Kosari, M.; Sheng, C. C.; Leong, O. S.; Xiao,
899   G.; Jiangyong, H. Pd-Decorated CuO Thin Film for Photodegradation of Acetaminophen
900   and Triclosan under Visible Light Irradiation. *Adv Mater Interfaces* **2018**, *5* (24),
901   1801440. https://doi.org/10.1002/ADMI.201801440.

902   (57) Wafi, A.; Szabó-Bárdos, E.; Horváth, O.; Makó, É.; Jakab, M.; Zsirka, B. Coumarin-
903   Based Quantification of Hydroxyl Radicals and Other Reactive Species Generated on
904   Excited Nitrogen-Doped TiO2. *J Photochem Photobiol A Chem* **2021**, *404*, 112913.
905   https://doi.org/10.1016/J.JPHOTOCHEM.2020.112913.

906   (58) Lee, S. K.; Sheridan, M.; Mills, A. Novel UV-Activated Colorímetric Oxygen Indicator.
907   *Chemistry of Materials* **2005**, *17* (10), 2744–2751.
908   https://doi.org/10.1021/CM0403863/ASSET/IMAGES/LARGE/CM0403863F00006.JPE
909   G.

910   (59) Wang, W.; Ye, M.; He, L.; Yin, Y. Nanocrystalline TiO2-Catalyzed Photoreversible Color
911   Switching. *Nano Lett* **2014**, *14* (3), 1681–1686.
912   https://doi.org/10.1021/NL500378K/SUPPL_FILE/NL500378K_SI_001.PDF.

913   (60) Kandambeth, S.; Mallick, A.; Lukose, B.; Mane, M. v.; Heine, T.; Banerjee, R.
914   Construction of Crystalline 2D Covalent Organic Frameworks with Remarkable Chemical
915   (Acid/Base) Stability via a Combined Reversible and Irreversible Route. *J Am Chem Soc*
916   **2012**, *134* (48), 19524–19527. https://doi.org/10.1021/JA308278W.

917   (61) Baig, N.; Madduluri, V. K.; Sah, A. K. Selective Oxidation of Organic Sulfides to
918   Sulfoxides Using Sugar Derived Cis-Dioxo Molybdenum(VI) Complexes: Kinetic and
919   Mechanistic Studies. *RSC Adv* **2016**, *6* (33), 28015–28022.
920   https://doi.org/10.1039/C6RA01087C.

921   (62) Borah, P.; Sreejith, S.; Anees, P.; Menon, N. V.; Kang, Y.; Ajayaghosh, A.; Zhao, Y.
922   Near-IR Squaraine Dye-Loaded Gated Periodic Mesoporous Organosilica for Photo-
923   Oxidation of Phenol in a Continuous-Flow Device. *Sci Adv* **2015**, *1* (8).
924   https://doi.org/10.1126/SCIADV.1500390/SUPPL_FILE/1500390_SM.PDF.

925   (63) Caudillo-Flores, U.; Rodríguez-Padrón, D.; Muñoz-Batista, M. J.; Kubacka, A.; Luque,
926   R.; Fernández-García, M. Facile Synthesis of B/g-C 3 N 4 Composite Materials for the
927   Continuous-Flow Selective Photo-Production of Acetone. *Green Chemistry* **2020**, *22* (15),
928   4975–4984. https://doi.org/10.1039/D0GC01326A.

929   (64) Prakash, B.; Singh, A.; Katoch, V.; Sharma, M.; Panda, J. J.; Sharma, J.; Ganguli, A. K.
930   Flow Synthesis and In-Channel Photocatalysis of Antimicrobially Active ZnS Quantum

931   Dots Using an Efficient Planar PMMA Microreactor. *Nano Express* **2020**, *1* (3), 030030.
932   https://doi.org/10.1088/2632-959X/ABCADF.

933 (65) Singh, A.; Baruah, A.; Katoch, V.; Vaghasiya, K.; Prakash, B.; Ganguli, A. K. Continuous
934   Flow Synthesis of Ag3PO4 Nanoparticles with Greater Photostability and Photocatalytic
935   Dye Degradation Efficiency. *J Photochem Photobiol A Chem* **2018**, *364*, 382–389.
936   https://doi.org/10.1016/J.JPHOTOCHEM.2018.05.017.

937 (66) Baruah, A.; Singh, A.; Sheoran, V.; Prakash, B.; Ganguli, A. K. Droplet-Microfluidics for
938   the Controlled Synthesis and Efficient Photocatalysis of TiO2 Nanoparticles. *Mater Res
939   Express* **2018**, *5* (7), 075019. https://doi.org/10.1088/2053-1591/AAAFED.

940 (67) Yang, H.; Coolman, R.; Karanjkar, P.; Wang, H.; Dornath, P.; Chen, H.; Fan, W.; Conner,
941   W. C.; Mountziaris, T. J.; Huber, G. The Effects of Contact Time and Coking on the
942   Catalytic Fast Pyrolysis of Cellulose. *Green Chemistry* **2017**, *19* (1), 286–297.
943   https://doi.org/10.1039/C6GC02239A.

944

945

946